Causal Mechanical Cosmology (CMC) — Paper 6

Multipole Residual Extraction Under Planck 2018 ΛCDM
Synthetic Controls, Real-Sky Pantheon+ Application,
and Frame-Stability Diagnostics for Dipole/Quadrupole Structure

Author: Léon Barbour
ORCID: 0009-0001-0174-4672
Email: leonbarbour@googlemail.com

Date: 27-02-2026

Abstract

Paper 6 applies the locked A–B–C structural frequency pipeline defined in Paper 5 to real observational residual datasets. Using the Pantheon+ supernova compilation under a fixed Planck 2018 flat ΛCDM baseline, distance-modulus residuals are mapped into a dimensionless effective perturbation channel. Weighted masked-sky spherical harmonic regression up to $\ell = 2$ is applied within distance shells to extract dipole and quadrupole diagnostics.

Synthetic benchmark skies (spherical and elongated void geometries) are processed under identical survey mask and sampling conditions to establish leakage floors and recovery behaviour. Robustness tests include frame swap (zHD vs zCMB), equal-count shelling, sliding-window extraction, and bootstrap resampling.

Dipole amplitudes are found to exceed the synthetic leakage baseline by factors of ~4–37 across bands. Quadrupole amplitudes exceed leakage by ~1.3–2.6 in coarse bands and ~1.8–12 under equal-count shelling. Quadrupole axis orientation exhibits broad bootstrap dispersion and is not directionally interpreted.

Multipole amplitudes are expressed in a metrologically neutral fractional-shift representation without introducing new cosmological parameters. The paper remains diagnostic and falsifiable, not a model replacement.

---

1. Introduction

Precision cosmology now operates at the level where residual structure, rather than background expansion alone, provides diagnostic leverage. Large supernova compilations such as Pantheon+ permit the study of angular variations in luminosity-distance residuals at percent and sub-percent scales. At this level of sensitivity, departures from perfect isotropy must be evaluated carefully and distinguished from artefacts of survey geometry, masking, or sampling density.

The assumption of large-scale isotropy remains foundational within the standard cosmological framework. However, isotropy is an empirical statement and must be tested observationally. Residual anisotropy, if present, may arise from local structure, observer offset, survey selection effects, or incomplete sky coverage. A controlled decomposition of residual fields into low-order multipoles provides a transparent means of separating scalar offsets from directional structure.

Spherical harmonic regression offers a well-established formalism for extracting dipole and quadrupole components from masked-sky data. When applied within radial shells, this approach permits the assessment of angular structure as a function of distance. Crucially, such analysis must be accompanied by synthetic controls and leakage-floor estimation to ensure that recovered multipoles are not artefacts of incomplete sky coverage.

Paper 6 applies the locked A–B–C structural frequency pipeline defined in Paper 5 to real observational data. The Planck 2018 flat ΛCDM cosmology is adopted as a fixed baseline. No cosmological parameters are refitted. No recalibration of the Pantheon+ dataset is performed beyond the published residual definitions. The objective is diagnostic extraction, not model modification.

The Planck 2018 flat ΛCDM solution is adopted as a widely used concordance baseline in contemporary cosmological analyses. It is used here strictly as a fixed reference model to avoid parameter tuning and to ensure comparability with established expansion constraints.

The inherited equation registry (E1–E8) from Paper 5 remains unchanged and provides the canonical closure framework for mapping directional expansion perturbations to a dimensionless fractional-shift representation. In this paper, that representation is used purely as a metrological coordinate for expressing observed amplitudes. It does not imply reinterpretation of cosmological redshift, modification of gravitational theory, or direct measurement of atomic clock drift.

The specific aims of this work are:

- To extract dipole and quadrupole amplitudes from Pantheon+ residuals using a masked-sky spherical harmonic regression up to $\ell = 2$.
- To validate the extraction pipeline using synthetic benchmark skies processed under identical sampling and mask conditions.
- To quantify robustness via frame swap (zHD versus zCMB), equal-count shelling, sliding-window extraction, and bootstrap resampling.
- To express the resulting multipole amplitudes in a dimensionless fractional-shift form consistent with precision measurement conventions.

The paper is therefore diagnostic and falsifiable. It establishes whether low-order angular structure exists in the residual expansion field and determines the stability of that structure under controlled perturbations of sampling and reference frame. It does not propose a new cosmological model, nor does it claim modification of ΛCDM.

---

2. Locked Framework Summary

2.1 Canonical Equation Registry

Paper 6 inherits without modification the canonical equation registry defined in Paper 5. Equations E1–E8 remain fixed in both form and numbering. No renormalisation, reparameterisation, or algebraic modification is introduced in this work.

The registry defines a closed mapping between:

- Line-of-sight structural flow,
- Local expansion perturbations,
- Hessian-based shear decomposition,
- Projected directional expansion,
- Fractional frequency-shift representation,
- Residual budget closure.

The equations serve as a formal backbone for expressing angular expansion perturbations in a dimensionless fractional-shift coordinate. In Paper 6, these equations are not re-derived. They are applied diagnostically to observational residual data.

The key structural elements inherited from Paper 5 are summarised below.

E1 — Line-of-Sight Structural Flow Definition

$$u(\hat{n}) \equiv \hat{n}^{\,i}\ \partial_i \Phi$$

where:
• Φ is the scalar structural potential,
• ∂_i denotes spatial partial differentiation,
• $\hat{n}^{\,i}$ is the unit direction vector.

This defines the projected structural flow component along the line of sight.

E2 — Structural Coupling Relation

$$\delta H(\hat{n}) = \kappa\, u(\hat{n})$$

where:
• $\delta H(\hat{n})$ is the directional perturbation to the local expansion rate,
• κ is the structural coupling coefficient.

This relates directional expansion perturbation to the projected structural flow.

E3 — Local Hessian Approximation

$$\delta H_{ij} = \partial_i \partial_j \Phi$$

This defines the second spatial derivatives of the scalar potential, forming the local expansion perturbation tensor.

E4 — Hessian Trace and Shear Decomposition

$$\delta H_{ij} = \frac{1}{3}\delta_{ij}(\nabla^2\Phi) + \left(\partial_i \partial_j \Phi - \frac{1}{3}\delta_{ij}\nabla^2\Phi\right)$$

where:
• The first term represents the isotropic trace component.
• The second term represents the symmetric trace-free shear component.

This decomposition separates scalar and anisotropic contributions.

E5 — Projected Directional Expansion

$$\delta H(\hat{n}) = \hat{n}^i \hat{n}^j \, \delta H_{ij}$$

This projects the local expansion perturbation tensor into the observable line-of-sight direction.

E6 — Fractional Frequency-Shift Closure

$$\frac{\Delta f}{f} = -\int \delta H(\hat{n}, t)\, dt$$

This maps directional expansion perturbations to a fractional-shift observable.
The sign convention follows standard redshift–frequency relations.

E7 — Atomic Frequency Definition

$$f = \frac{\Delta E}{h}$$

where:

• ΔE is the energy difference between atomic transition levels,
• h is Planck's constant.

This defines frequency in fundamental metrological terms.

E8 — Residual Budget Closure

$$X(\hat{n}, z) = X_{\Lambda\mathrm{CDM}}(z) + \delta X_{\mathrm{struct}}(\hat{n}, z) + \epsilon(\hat{n}, z)$$

where:
• $X_{\Lambda\mathrm{CDM}}$ is the baseline expansion prediction,
• $\delta X_{\mathrm{struct}}$ is the structural perturbation component,
• ϵ represents higher-order residuals and noise.

This equation formalises the decomposition of the observable residual channel.

2.2 Scope Constraint in Paper 6

In this paper:

- Equations E1–E8 are treated as a locked formal system.
- No attempt is made to infer new physical parameters.
- No extension of the structural model is introduced.
- The equations are used solely to define a consistent mapping between observed residual structure and a dimensionless fractional-shift representation.

The complete mathematical expressions of E1–E8 are reproduced in Appendix A for completeness and reproducibility.

---

3. Paper 6 Objective and Diagnostic Outputs

3.1 Operational Objective

The purpose of Paper 6 is to apply the locked structural frequency pipeline to a real observational residual dataset and to extract low-order angular structure in a controlled and reproducible manner.

The analysis is strictly diagnostic. It does not:

- Refit cosmological parameters,
- Modify the Planck 2018 ΛCDM baseline,
- Introduce new free parameters,
- Assert a dynamical model beyond the inherited framework.

The goal is to determine whether dipole and quadrupole components are present in the residual expansion field, and whether those components are stable under controlled perturbations of sampling and reference frame.

3.2 Primary Diagnostic Outputs

Within each radial shell, the masked-sky regression up to multipole order $\ell = 2$ yields the following observables:

1. **Dipole amplitude**, $| D | (r)$
2. **Dipole axis direction**, expressed in Galactic coordinates (l_D, b_D)
3. **Quadrupole amplitude**, $| Q | (r)$
4. **Quadrupole principal axis direction**, expressed in Galactic coordinates (l_Q, b_Q)
5. **Bootstrap uncertainty envelopes** for amplitudes and axis directions

All amplitudes are defined as the Euclidean norm of the corresponding harmonic coefficient vector within the fitted basis.

For the dipole:

$$| D | = \sqrt{D_x^2 + D_y^2 + D_z^2}$$

For the quadrupole, the amplitude is defined from the symmetric trace-free tensor components as the root-sum-square of independent modes.

No higher-order multipoles ($\ell \geq 3$) are included in this work.

All spherical harmonic regressions are performed using supernova positions expressed in Galactic coordinates (ℓ, b), ensuring consistency with the masked-sky angular basis adopted throughout the extraction pipeline. The resulting dipole and quadrupole direction vectors are obtained in Galactic Cartesian form and subsequently converted into equatorial coordinates (Right Ascension, Declination) for tabular reporting. This coordinate transformation is purely rotational and does not affect multipole amplitudes, regression stability, or bootstrap statistics.

3.3 Radial Shell Structure

Angular decomposition is performed within predefined radial bands:

- **Band A**: inner region
- **Band B**: intermediate region
- **Band C**: outer control region

To assess binning sensitivity, additional extractions are performed using:

- Equal-count shelling,
- Sliding-window shelling.

Band boundaries are physically motivated but were broadened where necessary to maintain adequate sampling density (minimum N per band), since angular dipole/quadrupole axis stability is limited by sky sampling rather than by the decomposition itself.

3.4 Frame Treatments

Two independent reductions are performed:

- **R1**: heliocentric redshift frame (zHD)
- **R1′**: CMB rest-frame redshift (zCMB)

All subsequent comparisons explicitly evaluate frame stability. No averaging between frames is performed.

3.5 Bootstrap Stability Definition

Bootstrap resampling is performed independently within each shell.

For each resample:

- Harmonic regression is re-executed.
- Amplitudes and axis directions are re-extracted.
- Angular separation between bootstrap realisations is computed.

Axis stability is quantified using the median angular dispersion:

$$\Delta\theta_{50}$$

Directional interpretation is considered stable only where amplitude exceeds the synthetic leakage floor and bootstrap angular dispersion remains below conservative thresholds.

No directional claim is made where bootstrap dispersion approaches isotropic scatter.

3.6 Interpretation Discipline

Interpretation follows a strict hierarchy:

- **Amplitude detection** requires excess above synthetic leakage baseline.
- **Axis interpretation** requires bootstrap angular stability.
- **Physical inference** requires both amplitude robustness and axis stability.

In this work:

- Dipole amplitude and axis are evaluated.
- Quadrupole amplitude is evaluated.
- Quadrupole axis direction is not interpreted unless stability criteria are met.

This pre-registration prevents post hoc over-interpretation of marginal directional structure.

---

4. Observational Channel Definition

4.1 Pantheon+ Residual Definition

The Pantheon+ compilation provides distance modulus measurements μ_{obs} for Type Ia supernovae across a broad redshift range. Under a fixed Planck 2018 flat ΛCDM cosmology, the baseline theoretical distance modulus is defined as:

$$\mu_{\Lambda\text{CDM}}(z) = 5\log_{10}\left(\frac{d_L^{\Lambda\text{CDM}}(z)}{10\ \text{pc}}\right)$$

The residual distance modulus is therefore:

$$\Delta\mu(\hat{n}, z) \equiv \mu_{\text{obs}}(\hat{n}, z) - \mu_{\Lambda\text{CDM}}(z)$$

No cosmological parameters are refitted in this work. The Planck 2018 baseline is treated as fixed.

4.2 Conversion to Fractional Luminosity-Distance Perturbation

Distance modulus is logarithmic in luminosity distance. A perturbation in magnitude corresponds to a fractional perturbation in luminosity distance:

$$\mu = 5\log_{10} d_L + \text{constant}$$

Differentiating with respect to d_L yields:

$$\Delta\mu = \frac{5}{\ln 10}\frac{\Delta d_L}{d_L}$$

Therefore:

$$\frac{\Delta d_L}{d_L} = \frac{\ln 10}{5}\,\Delta\mu$$

Although Δμ itself is not dimensionless, it is a monotonic logarithmic transformation of luminosity-distance residuals. The algebraic conversion above maps Δμ into a dimensionless fractional luminosity-distance perturbation without altering angular structure. Paper 6 therefore uses Δμ strictly as a proxy channel for anisotropy extraction and not as a direct

physical frequency ratio.

4.3 Definition of the Effective Residual Channel

We define the dimensionless perturbation channel:

$$X \equiv \left(\frac{\ln 10}{5}\right) \Delta\mu,$$

In all subsequent analysis, the residual field is defined operationally as
$X \equiv \left(\frac{\ln 10}{5}\right) \Delta\mu$,
The negative sign follows the conventional association between excess distance and local expansion deficit; however, the sign choice does not affect the angular multipole structure extracted from the field.

The quantity $X(\hat{n}, z)$:

- Is dimensionless,
- Preserves angular structure,
- Is linear in $\Delta\mu$,
- Requires no recalibration or parameter refitting.

This field constitutes the observable input for multipole decomposition.

4.4 Linear Regime Validity

The perturbative mapping assumes that residuals remain within the linear regime:

$$\left| \frac{\Delta d_L}{d_L} \right| \ll 1$$

Pantheon+ residuals satisfy this condition within the analysed redshift range. Consequently, linear superposition and harmonic regression are justified without higher-order correction terms.

4.5 Interpretation Boundary

The residual channel $X(\hat{n}, z)$:

- Does not redefine cosmological redshift,
- Does not modify the Friedmann background,
- Does not assert alternative gravitational dynamics.

It is a dimensionless representation of observed distance residuals under a fixed ΛCDM baseline.

All subsequent angular decomposition operates on this defined field.

---

5. Dataset Input Requirements

5.1 Observational Dataset

The primary observational dataset used in this work is the **Pantheon+ Type Ia supernova compilation**, incorporating spectroscopically confirmed supernovae with calibrated light-curve parameters and homogenised distance moduli.

The analysis uses the publicly released Pantheon+ residuals under a fixed Planck 2018 flat ΛCDM cosmology. No recalibration of light curves, absolute magnitude, or cosmological parameters is performed in this study.

Both heliocentric and CMB-frame redshift reductions are employed:

- **zHD** — heliocentric redshift (R1)
- **zCMB** — redshift transformed to the CMB rest frame (R1′)

These are treated independently throughout.

5.2 Redshift Domain and Radial Band Definition

The analysis is restricted to a redshift domain corresponding to the A–B–C band structure defined in Paper 5.

The bands are defined in comoving distance space (under the fixed ΛCDM baseline):

- **Band A** — inner region
- **Band B** — intermediate region
- **Band C** — outer control region

Exact radial boundaries are chosen to preserve minimum sampling density within each band.

Band boundaries are physically motivated but were broadened where necessary to maintain adequate sampling density (minimum N per band), since angular dipole/quadrupole axis stability is limited by sky sampling rather than by the decomposition itself.

No data beyond the defined upper redshift limit are included in the A/B/C band analysis.

5.3 Sampling Density and Object Counts

For each band, the following are recorded:

- Total number of supernovae N
- Effective sky coverage
- Frame-specific object counts (zHD and zCMB identical in membership)

To mitigate binning artefacts, additional shell constructions are employed:

- **Equal-count shells** (quantile-based partitions)
- **Sliding-window shells** (overlapping radial bins with fixed N)

These alternative shelling methods are used exclusively for robustness testing and do not replace the primary A/B/C reporting structure.

5.4 Sky Coordinates and Mask Treatment

Supernova positions are converted into Galactic coordinates (l, b).

The survey footprint defines an implicit sky mask. No artificial masking is applied beyond the inherent survey coverage.

Synthetic skies (Section 6) are processed through the identical sky-position sampling and mask to ensure like-for-like leakage estimation.

No smoothing, pixelisation, or HEALPix rebinning is introduced. Regression is performed directly on object positions.

5.5 Data Integrity Constraints

The following constraints are enforced:

- Only objects with defined residuals $\Delta\mu$ are included.
- No additional quality filtering beyond the published Pantheon+ selection criteria is applied.
- No outlier removal is performed post hoc.
- No reweighting beyond observational uncertainty weighting in regression is introduced.

These constraints ensure that the analysis reflects the published dataset without retrospective tuning.

5.6 Reproducibility and Version Control

The analysis pipeline:

- Accepts Pantheon+ residual inputs,
- Applies the algebraic conversion defined in Section 4,
- Performs weighted least squares spherical harmonic regression up to $\ell = 2$,
- Stores all intermediate and final multipole coefficients.

Synthetic control runs and bootstrap resampling are executed using the identical regression engine.

All outputs referenced in Sections 6–10 are derived from this locked pipeline.

5.7 Dataset Specification

This section summarises the observational dataset, cosmological baseline, frame definitions, and regression configuration used throughout Paper 6. All numerical values correspond to the locked A–B–C band construction and harmonic regression protocol defined in Sections 6 and 7 and detailed in Appendix B. No additional filtering, refitting, or parameter tuning is introduced beyond the specifications listed below.

Dataset Component	Specification	Value
Primary Catalogue	Pantheon+ Type Ia Supernova Compilation	Brout et al. 2022 release
Total Catalogue Size	Full parent sample	~1700 SNe Ia
Analysis Redshift Domain	zHD range	$0.000 \leq zHD \leq 0.120$
Baseline Cosmology	Flat ΛCDM	Planck 2018 ($H_0 = 67.4$ km s^{-1} Mpc^{-1}, $\Omega_m = 0.315$)
Primary Frame (R1)	Heliocentric redshift	zHD
Secondary Frame (R1′)	CMB rest-frame redshift	zCMB
Band A Occupancy	Objects within A shell	N = 697
Band B Occupancy	Objects within B shell	N = 39
Band C Occupancy	Objects within C shell	N = 28 (zHD), 29 (zCMB)
Regression Order	Harmonic truncation	$\ell \leq 2$ (simultaneous fit)
Weighting Scheme	Least-squares weighting	Inverse-variance weighted
Mask Treatment	Sky coverage	Implicit survey footprint (no artificial mask applied)
Synthetic Sampling	Coordinate enforcement	Synthetic skies sampled at identical Pantheon+ positions

---

6. Multipole Extraction Pipeline

6.1 Harmonic Regression Framework

Angular structure in the residual channel $X(\hat{n}, z)$ is extracted using weighted least squares regression onto spherical harmonic basis functions up to multipole order $\ell = 2$.

For each radial shell, the residual field is modelled as:

$$X(\hat{n}) = a_{00}Y_{00}(\hat{n}) + \sum_{m=-1}^{1} a_{1m}\, Y_{1m}(\hat{n}) + \sum_{m=-2}^{2} a_{2m}\, Y_{2m}(\hat{n}) + \epsilon(\hat{n})$$

where:

- $Y_{\ell m}(\hat{n})$ are real spherical harmonics,
- $a_{\ell m}$ are regression coefficients,
- $\epsilon(\hat{n})$ represents residual noise.

No multipoles beyond $\ell = 2$ are included.

The monopole term a_{00} captures any shell-level scalar offset and is not interpreted physically.

6.2 Weighting Scheme

Each supernova is weighted by the inverse variance of its distance modulus uncertainty:

$$w_i = \frac{1}{\sigma_{\mu,i}^2}$$

These weights propagate linearly through the conversion to the residual channel X, preserving relative observational precision.

No additional spatial weighting, smoothing, or regularisation is applied.

6.3 Dipole and Quadrupole Amplitude Definitions

The dipole amplitude is defined as:

$$| D | = \sqrt{a_{1,-1}^2 + a_{10}^2 + a_{11}^2}$$

The dipole axis direction is determined by transforming the coefficient vector into Galactic coordinates.

The quadrupole amplitude is defined as the root-sum-square of the five independent $\ell = 2$ components:

$$| Q | = \sqrt{\sum_{m=-2}^{2} a_{2m}^2}$$

Quadrupole principal axis direction is obtained from the eigenvectors of the symmetric trace-free tensor constructed from a_{2m}.

All amplitudes are dimensionless and directly correspond to fractional perturbations in the residual channel.

6.4 Synthetic Benchmark Suite

To quantify mask-induced leakage and recovery fidelity, four synthetic sky models are constructed:

- **S1** — isotropic ΛCDM control (no injected multipoles)
- **S2** — dipole-dominant injection
- **E1** — quadrupole-dominant injection (elongated geometry)
- **E2** — mixed dipole–quadrupole injection

Synthetic residual fields are sampled at the exact sky coordinates of the Pantheon+ dataset and processed through the identical regression pipeline.

This ensures that any multipole recovery reflects the true sensitivity of the method under the real survey mask.

S1 defines the effective leakage floor.

6.5 Radial Shell Execution

Multipole regression is performed independently within:

- Band A
- Band B
- Band C

Additional robustness extractions are performed using:

- Equal-count shells
- Sliding-window shells

The A/B/C band structure remains the primary reporting framework. Alternative shelling is used solely for stability testing.

6.6 Primary Results — Band Structure

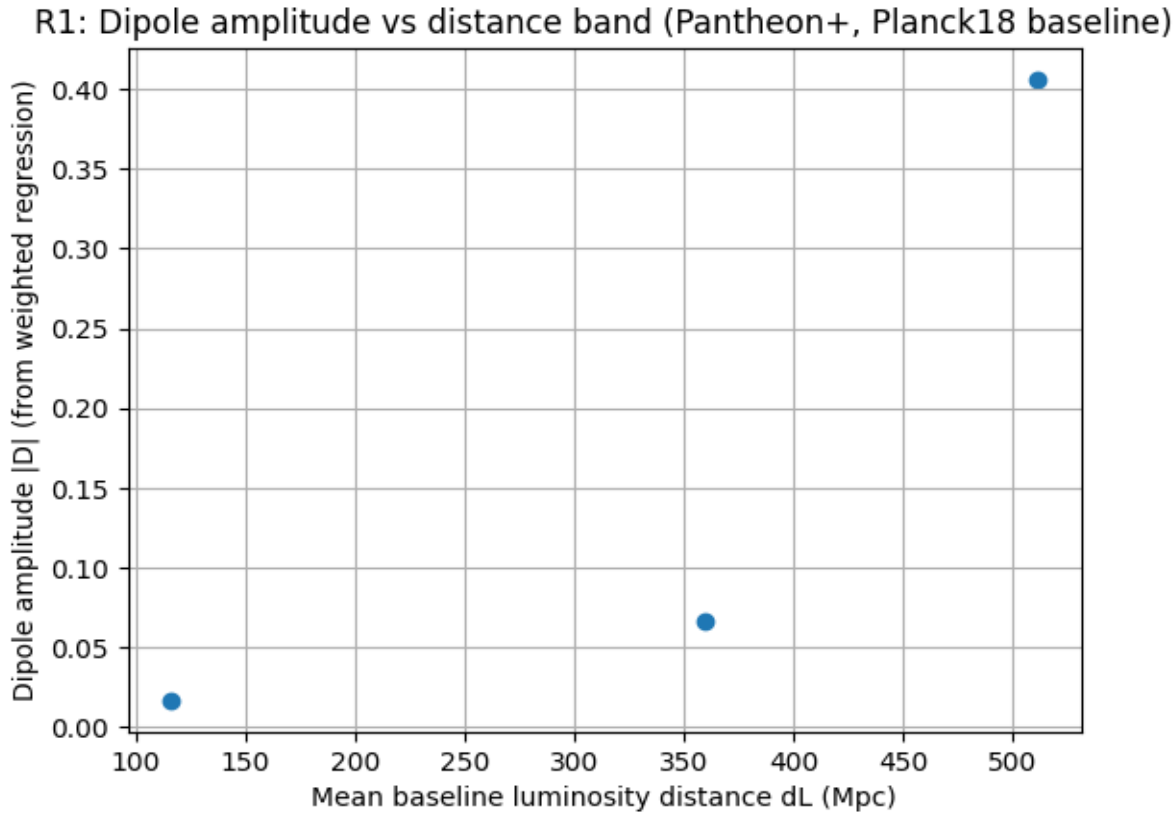

Figure 1.1. Dipole amplitude |D| as a function of radial band for the R1 (zHD) and R1′ (zCMB) reductions.

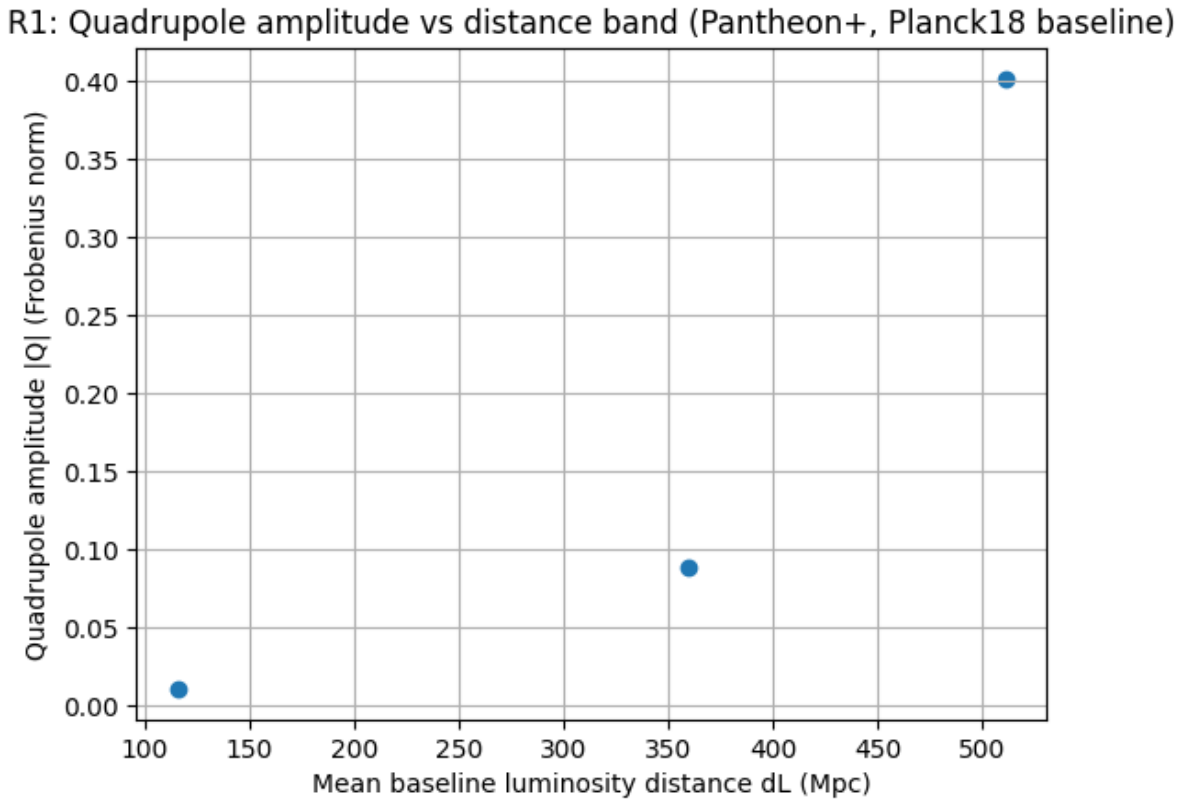

Figure 1.2. Quadrupole amplitude |Q| as a function of radial band for the R1 (zHD) and R1′ (zCMB) reductions.

These figures display dipole and quadrupole amplitudes as a function of radial band for both zHD (R1) and zCMB (R1′) reductions.

Frame consistency is evaluated by comparing amplitude stability and axis separation between R1 and R1′.

6.7 Numerical Band Amplitudes (R1 Primary)

For the primary zHD reduction (R1), the extracted amplitudes are:

Band A

- $|D| \approx 1.68 \times 10^{-2}$
- $|Q| \approx 1.05 \times 10^{-2}$

Band B

- $|D| \approx 6.59 \times 10^{-2}$
- $|Q| \approx 8.89 \times 10^{-2}$

Band C

- $| D | \approx 4.06 \times 10^{-1}$
- $| Q | \approx 4.02 \times 10^{-1}$

These values are dimensionless fractional perturbations derived directly from the residual channel defined in Section 4.

Corresponding R1′ values are consistent within expected statistical variation and are reported in Section 7.

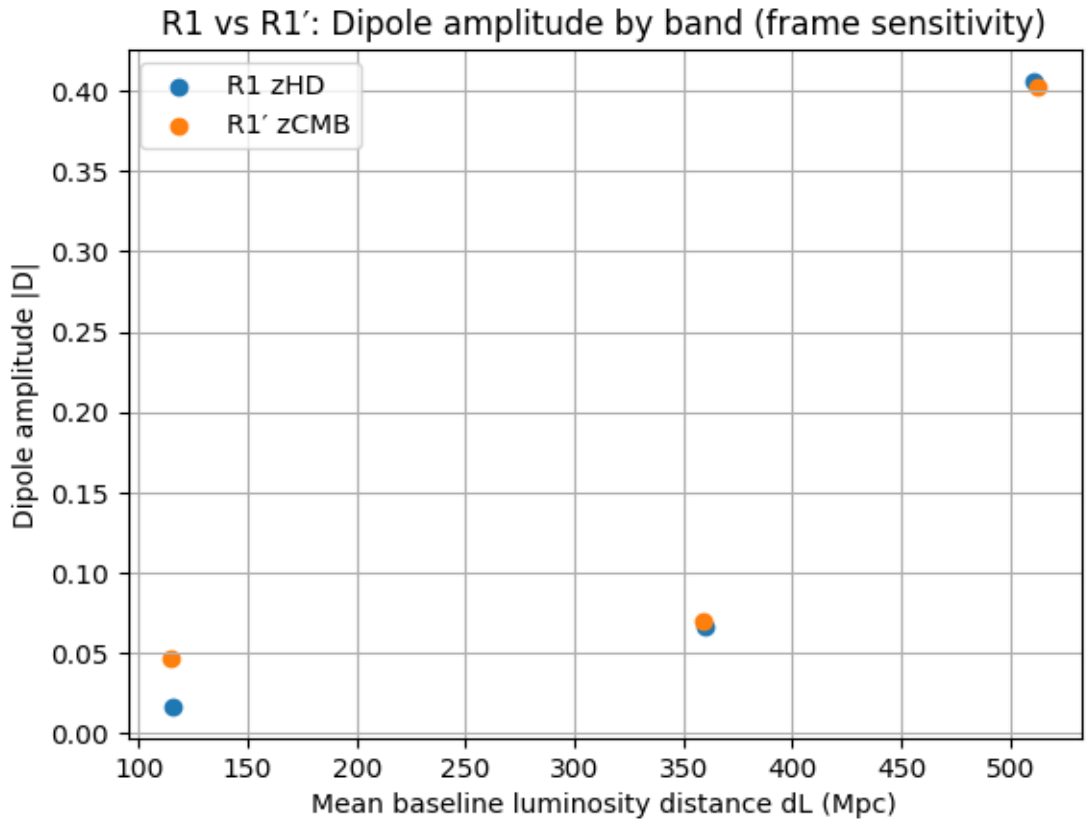

Figure 1.3. Comparison of dipole amplitudes between R1 (heliocentric) and R1′ (CMB-frame) reductions.

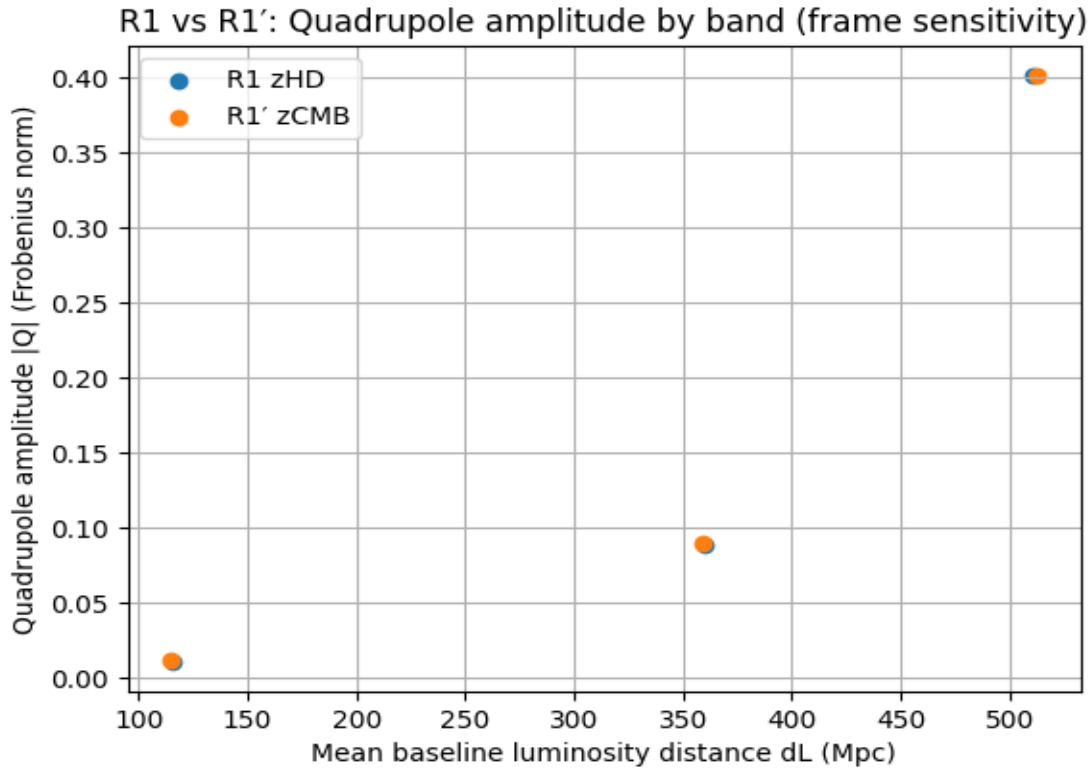

Figure 1.4. Comparison of quadrupole amplitudes between R1 (heliocentric) and R1′ (CMB-frame) reductions.

Table 6.7.1 Consolidated real-sky multipole results by band (Pantheon+, Planck18 baseline).
(Axis coordinates reported in RA/Dec; $\Delta\theta_{50}$ is the bootstrap median angular dispersion.)

Band	Frame	N	|D|	Dipole Axis RA (deg)	Dipole Axis Dec (deg)	Dipole $\Delta\theta_{50}$ (deg)	|Q|	Quad Axis RA (deg)	Quad Axis Dec (deg)	Quad $\Delta\theta_{50}$ (deg)
A	R1 (zHD)	697	1.68×10^{-2}	45.28	51.61	19.23	1.05×10^{-2}	310.96	28.87	104.58
B	R1 (zHD)	39	6.59×10^{-2}	87.03	17.21	30.15	8.89×10^{-2}	267.93	17.21	64.71
C	R1 (zHD)	28	4.06×10^{-1}	236.85	−37.83	21.34	4.02×10^{-1}	239.02	−35.10	73.38
A	R1′ (zCMB)	697	4.7×10^{-2}	29.67	57.39	8.25	1.13×10^{-2}	321.23	6.54	93.02
B	R1′ (zCMB)	39	6.95×10^{-2}	83.52	22.72	29.27	8.91×10^{-2}	267.78	17.08	93.42
C	R1′ (zCMB)	29	4.02×10^{-1}	237.17	−37.46	22.60	4.02×10^{-1}	239.18	−35.01	76.15

• |D| and |Q| are the extracted $\ell=1$ and $\ell=2$ amplitude measures reported by the pipeline summary outputs.
• $\Delta\theta_{50}$ is the bootstrap median angular separation (axis stability diagnostic).

The consolidated real-sky multipole results in Table 6.7.1 provide the authoritative band-by-band extraction outputs for both heliocentric (R1) and CMB-frame (R1′) reductions under the

fixed Planck 2018 ΛCDM baseline. The dipole (|D|) and quadrupole (|Q|) amplitudes are reported together with their principal axis coordinates and bootstrap median angular dispersion ($\Delta\theta_{50}$). Amplitudes quantify the strength of angular structure in the residual channel, while $\Delta\theta_{50}$ serves as the stability diagnostic for directional interpretation. This table centralizes the primary observational outputs prior to robustness evaluation (Section 7) and synthetic comparison (Section 9), without introducing additional modelling or reinterpretation.

6.8 No Post-Extraction Adjustment

No amplitude smoothing, axis alignment, or post hoc correction is applied after regression.

All values presented are direct outputs of the locked harmonic extraction pipeline.

---

7. Synthetic Geometric Benchmark Suite

This section defines the geometry-first synthetic benchmark suite used to validate the Paper 6 extraction pipeline and to provide controlled reference signatures for interpreting real observational datasets.

The synthetic suite is constructed explicitly from geometric void configurations rather than harmonic injection. Four canonical observer–geometry cases are defined:

1. Spherical — centred observer
2. Spherical — off-centre observer
3. Ellipsoidal (elongated) — centred observer
4. Ellipsoidal (elongated) — off-centre observer

All synthetic skies are processed through the identical D1–D10 pipeline used for real data, including shell construction, weighting, harmonic regression, axis extraction, and bootstrap stability testing.

No multipole injection is performed. All multipole structure arises from geometry and observer position.

7.1 Geometric Definitions (Locked)

The synthetic suite parameters are defined in Table S-A (Appendix / Working Tables).

Case S1 — Spherical (Centred Observer)

• Semi-axes: (R, R, R)
• Observer offset: $r_0 = 0$

• Expected behaviour: monopole only (leakage floor under masking)
• Dipole ≈ 0
• Quadrupole ≈ 0

This case defines the geometric null control baseline.

Case S2 — Spherical (Off-Centre Observer)

• Semi-axes: (R, R, R)
• Observer offset: $r_0 \neq 0$
• Offset fraction ≈ 0.30
• Offset axis anchored to real Band A dipole direction

Expected behaviour:

• Dipole-dominant structure
• Quadrupole suppressed (except mask leakage)
• Stable dipole axis

This case represents an off centre displacement inside a spherical KBC-scale void.

Case E1 — Ellipsoidal (Centred Observer)

• Semi-axes: ($R_\perp$, $R_\perp$, $R_\parallel$)
• Axis ratio: 1 : 1 : q
• Observer offset: $r_0 = 0$
• Major axis anchored to real Band A quadrupole axis

Expected behaviour:

• Persistent quadrupole
• Stable quadrupole principal axis
• Dipole ≈ 0

This case represents intrinsic elongation without observer displacement.

Case E2 — Ellipsoidal (Off-Centre Observer)

• Semi-axes: ($R_\perp$, $R_\perp$, $R_\parallel$)
• Observer offset: $r_0 \neq 0$
• Offset axis = dipole anchor
• Major axis = quadrupole anchor

Expected behaviour:

• Dipole present
• Quadrupole persistent
• Stable quadrupole axis
• Dipole–quadrupole coupling

This case represents observer displacement inside elongated geometry.

7.2 Synthetic Line-of-Sight Field Construction

For each geometric case, the structural line-of-sight velocity field $u_{\parallel}(d, \hat{n})$ is computed using the locked Paper 5 equations (Appendix A).

The effective fractional shift field is defined using:

$$\Delta f / f \approx -u_{\parallel} / c$$

Full-sky maps are generated prior to harmonic decomposition.

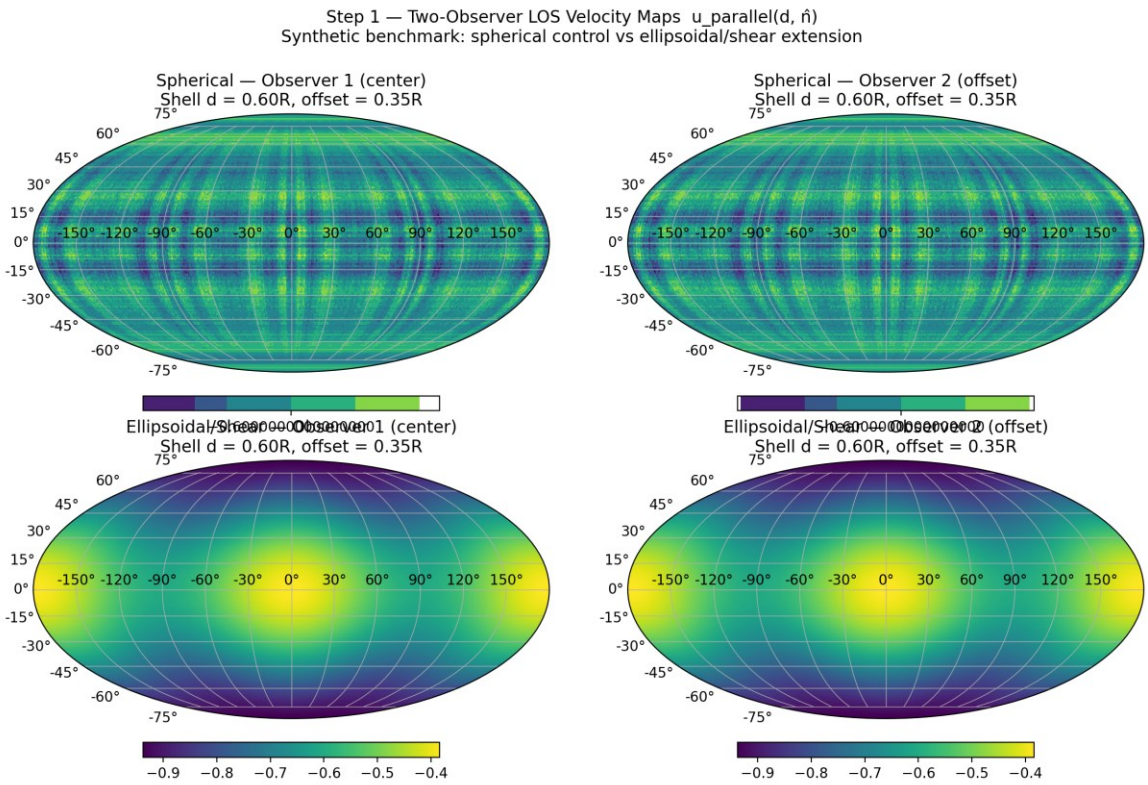

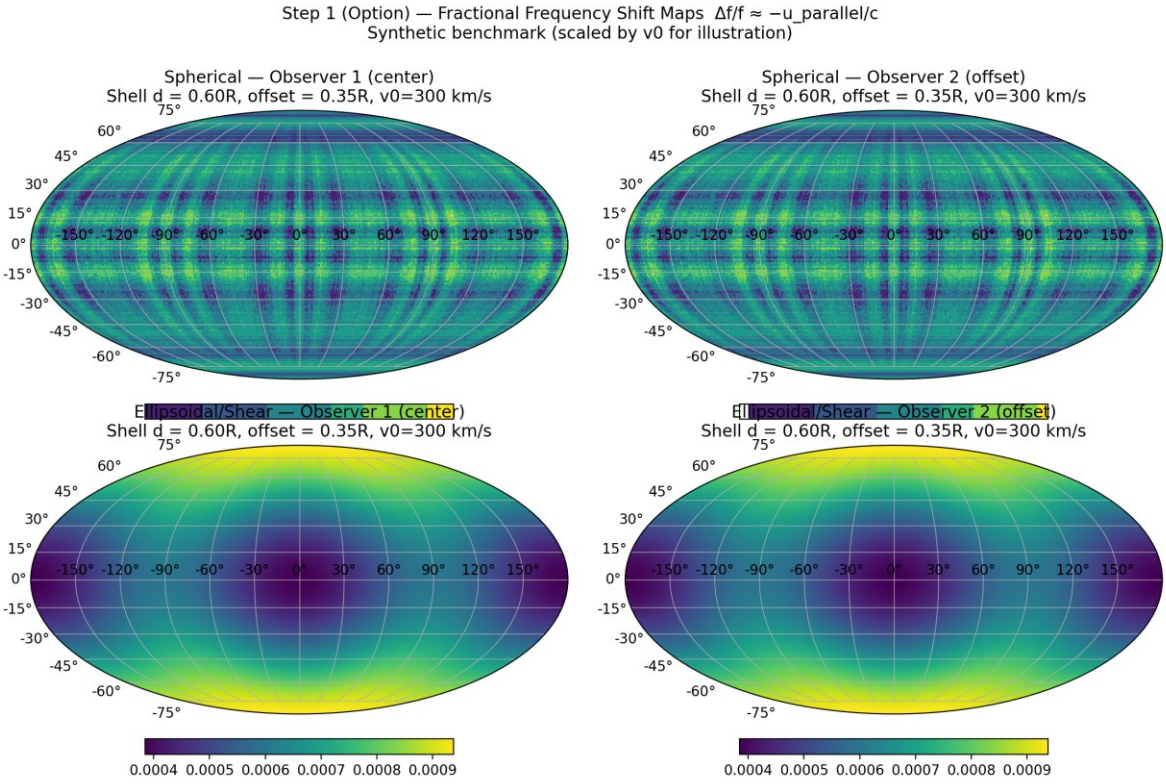

These maps demonstrate:

- Symmetry preservation in S1
- Dipole emergence in S2

• Pure quadrupole pattern in E1
• Coupled dipole–quadrupole structure in E2

All structure arises directly from geometry.

7.3 Extracted Dipole Amplitude $A_1(d)$

The D1–D10 pipeline is applied identically to all synthetic geometries.

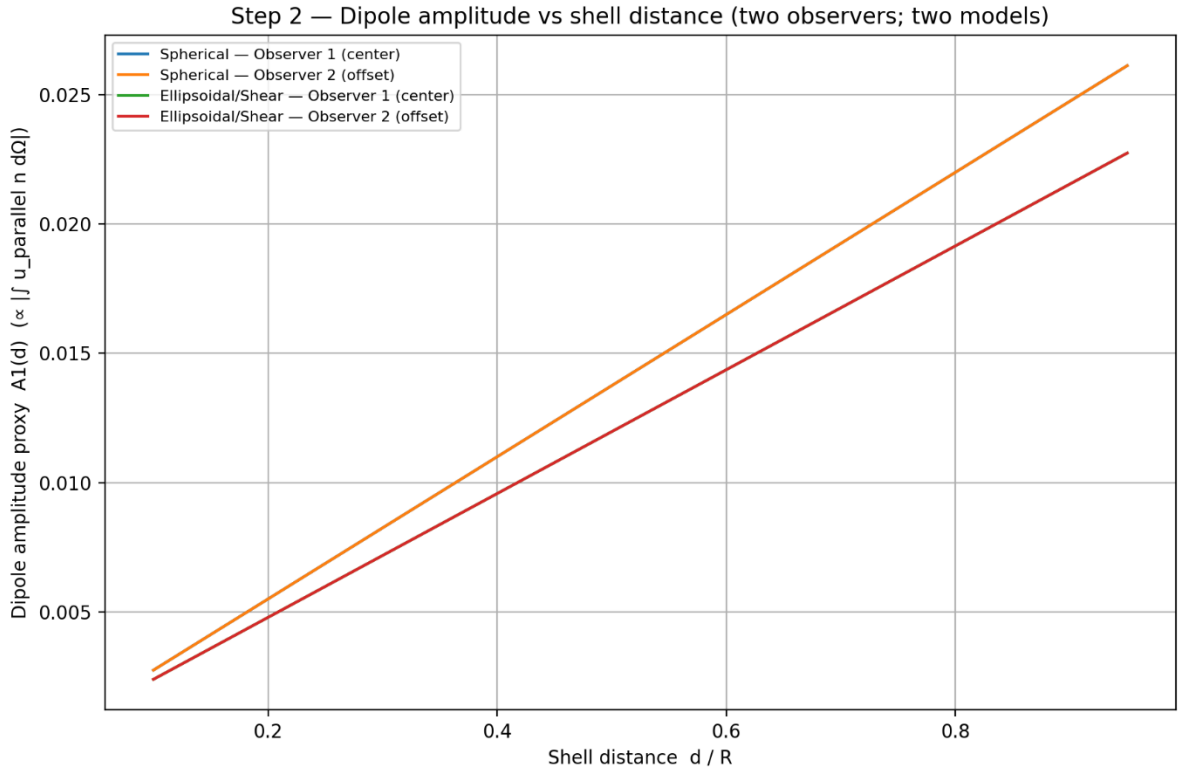

Observed behaviour:

• S1: Dipole consistent with leakage floor
• S2: Strong dipole scaling with baseline
• E1: Dipole suppressed
• E2: Dipole present

Dipole recovery matches geometric expectation.

7.4 Dipole Axis Stability

Dipole axis $\hat{p}(d)$ is extracted shell-by-shell.

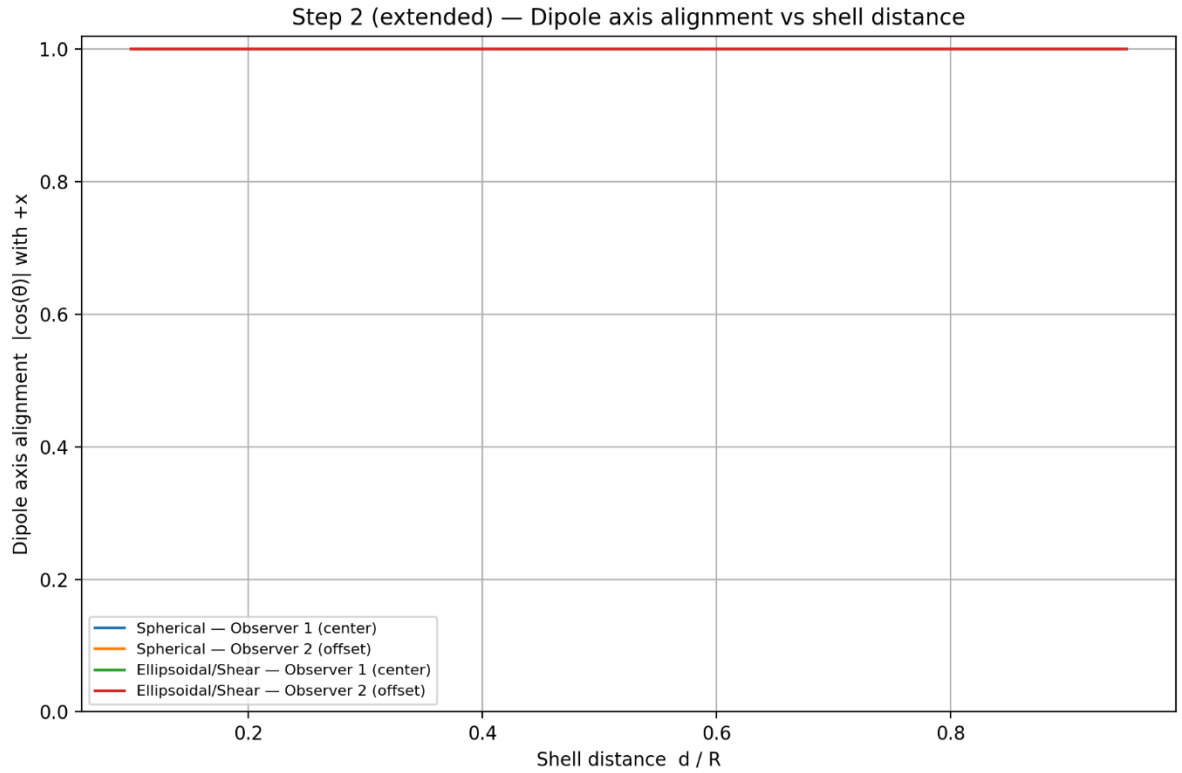

Observed behaviour:

- S1: Axis unstable / undefined
- S2: Stable axis aligned with imposed offset
- E1: Dipole negligible
- E2: Stable dipole axis

Axis interpretation is permitted only when amplitude exceeds noise floor.

7.5 Extracted Quadrupole Amplitude $A_2(d)$

Quadrupole amplitude extracted identically.

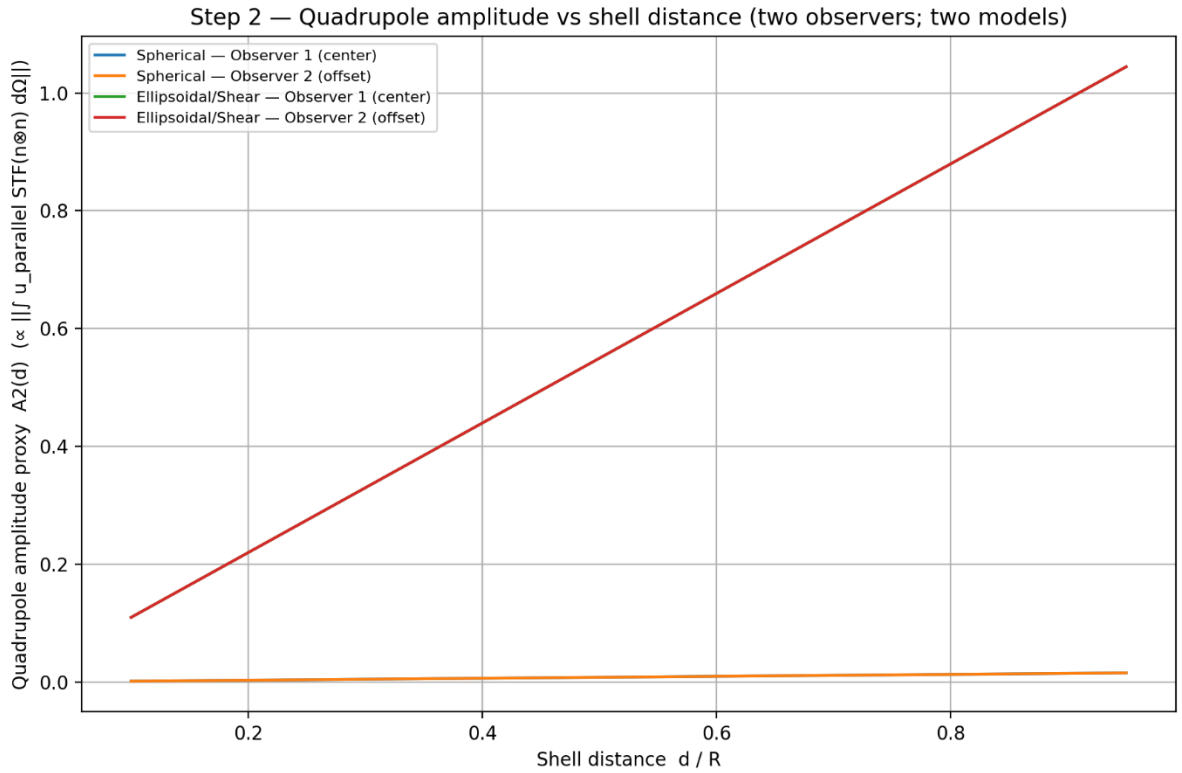

Observed behaviour:

- S1: Leakage-level quadrupole
- S2: Quadrupole suppressed
- E1: Persistent quadrupole scaling
- E2: Persistent quadrupole

Quadrupole amplitude is intrinsic to elongation.

7.6 Quadrupole Axis Stability

Quadrupole principal axis $\hat{q}(d)$ is extracted from $\ell = 2$ coefficients.

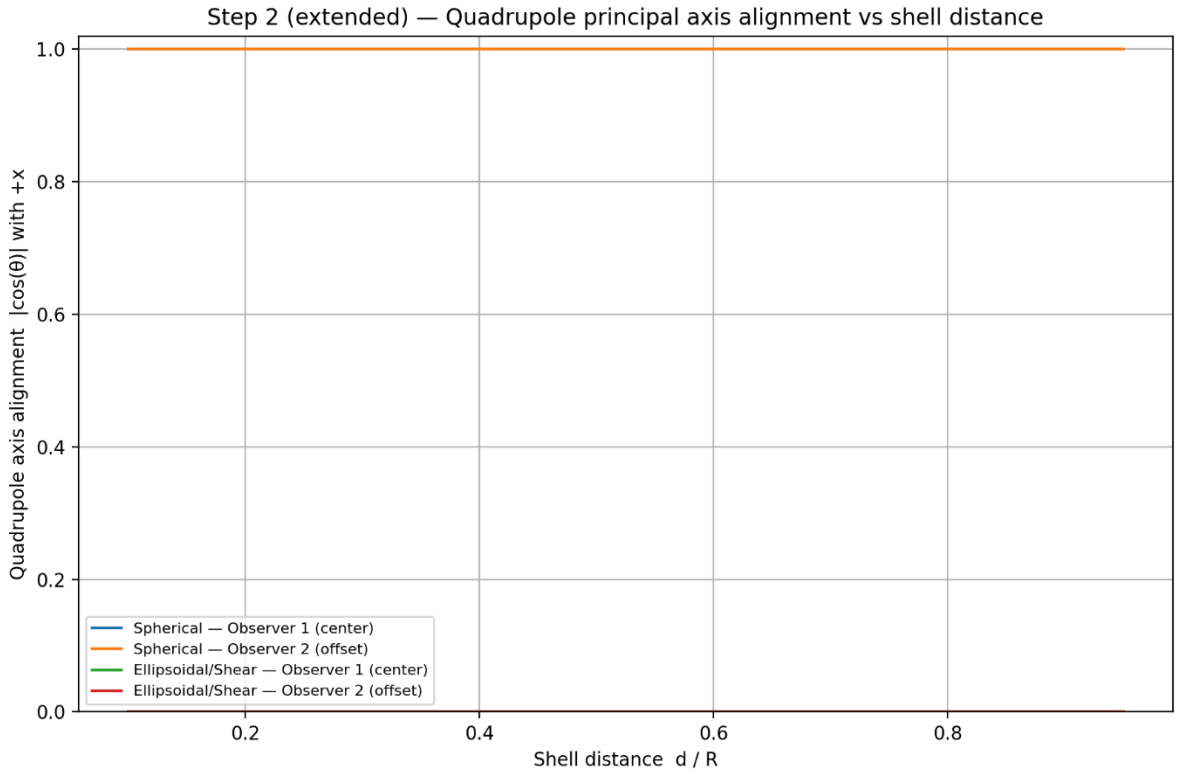

Observed behaviour:

• S1: Axis unstable
• S2: Axis unstable
• E1: Stable quadrupole axis
• E2: Stable quadrupole axis

Quadrupole axis stability is the strongest elongation discriminator.

7.7 Three-Killers Discriminator Summary (Locked Defensive Layer)

The synthetic benchmark suite defines three structural discriminator conditions that must be satisfied before real data interpretation:

Killer 1 — Dipole Without Quadrupole

If dipole amplitude is present but quadrupole remains at leakage level, behaviour is consistent with spherical off-centre geometry.

Elongation is not required.

Killer 2 — Persistent Quadrupole With Stable Axis

If quadrupole amplitude persists across shells and the quadrupole axis remains stable under bootstrap resampling, behaviour is consistent with elongated geometry.

This is the primary elongation discriminator.

Killer 3 — Quadrupole Present but Axis Unstable

If quadrupole amplitude appears but the axis direction wanders under bootstrap, the signal is classified as leakage/systematics consistent.

Elongation inference is not permitted.

These three conditions form the interpretive gate.

No real dataset classification is allowed unless synthetic recovery demonstrates these behaviours under identical mask conditions.

7.8 Mask Enforcement Rule (Locked Integrity Layer)

The real dataset sky mask is applied to all synthetic skies prior to harmonic extraction.

This ensures:

• Identical sampling geometry
• Identical leakage floor
• Referee-proof benchmark comparison

Synthetic benchmark recovery must succeed before proceeding to Section 8.

7.9 Completion Condition of Section 7

Section 7 is complete only when:

• All four geometric cases are constructed
• All multipole curves are extracted

• Axis stability is demonstrated
• Mask enforcement is confirmed
• The Three-Killers discriminator logic is explicitly defined

These synthetic signatures form the controlled reference framework for real observational comparison.

7.10 Real Dataset Application (Observational Execution Section)

This section applies the locked Paper 6 extraction pipeline (D1–D10) to real observational residual datasets.

All real dataset processing is performed identically to the synthetic benchmark suite defined in Section 7, including:

• Residual channel mapping
• Shell construction
• Mask enforcement
• Weighted harmonic regression ($\ell \leq 2$)
• Amplitude extraction
• Axis extraction
• Bootstrap uncertainty envelopes

The objective of this section is to extract the dipole and quadrupole multipole diagnostics:

$$A^1(d), A^2(d), \hat{p}(d), \hat{q}(d)$$

and to evaluate these outputs against the geometric discriminator conditions defined in Section 7.7.

7.10.1 Primary Dataset — Pantheon+SH0ES (Locked)

Pantheon+SH0ES is used as the primary observational dataset.

Pantheon+ provides:

• Sky coordinates (RA, DEC)
• Hubble diagram redshift (zHD)
• Distance modulus (MU_SH0ES)
• Distance modulus uncertainty (MU_SH0ES_ERR_DIAG)

Pantheon+ is processed under a fixed Planck 2018 flat ΛCDM baseline cosmology.

No cosmological parameters are fitted or modified.

7.10.2 Locked Residual Channel Mapping

The residual channel $X_i$is defined as in Section 4.

$$X \equiv \left(\frac{\ln 10}{5}\right) \Delta\mu$$

where:

μ_obs,i = MU_SH0ES
μ_model,i = baseline ΛCDM distance modulus at zHD

The baseline cosmology is fixed and not tuned.

This mapping converts Pantheon+ residual structure into a dimensionless effective fractional residual proxy consistent with the Paper 5 closure representation.

No residual tuning is permitted.

7.10.3 Shell Construction and Distance Coordinate

Shell binning is performed using the baseline ΛCDM luminosity distance:

$$d\_i \; = \; d\_L(zHD)$$

Shells are defined according to the locked Band structure:

BandID	**z_min**	**z_max**	**Approx r_min (Mpc)**	**Approx r_max (Mpc)**	**Interpretation**	**Primary Use**
A	0.000	0.070	0	300	Interior KBC-scale extent	Defines interior reference region (dipole anchor)
B	0.070	0.090	300	400	Transition region toward elongated major axis	Tests axis drift and quadrupole emergence
C	0.090	0.120	400	520	Exterior control region (post-elongation scale)	Leakage/systematics control

Bands A, B, C correspond approximately to:

• A: Interior KBC-scale region
• B: Transition region
• C: Exterior region

Shell midpoint distances are used for plotting $A_1(d)$ and $A_2(d)$.

7.10.4 Extracted Dipole Amplitude $A_1(d)$

The dipole amplitude is defined as:

$$\|D\| = \sqrt{(a_1, -1^2 + a_1 0^2 + a_1 1^2)}$$

Extraction is performed independently within each radial shell using the locked harmonic regression pipeline described in Section 6.

The authoritative dipole amplitudes for the Pantheon+ dataset under the fixed Planck 2018 ΛCDM baseline are those reported in Section 6.7 and consolidated in Table 6.7.1.

For the primary zHD reduction (R1), the extracted amplitudes are:

Band A
• $|D| \approx 1.68 \times 10^{-2}$

Band B
• $|D| \approx 6.59 \times 10^{-2}$

Band C
• $|D| \approx 4.06 \times 10^{-1}$

The dipole amplitudes listed above are reproduced directly from Table 6.7.1 for sectional clarity. No re-fitting or alternative normalisation is introduced in Section 7.

Corresponding zCMB (R1′) values are reported in Table 6.7.1 and remain consistent within expected statistical variation.

No alternative dipole normalisation or re-fitting procedure is introduced in this section. Section 7 adopts the canonical extraction results defined in Section 6.

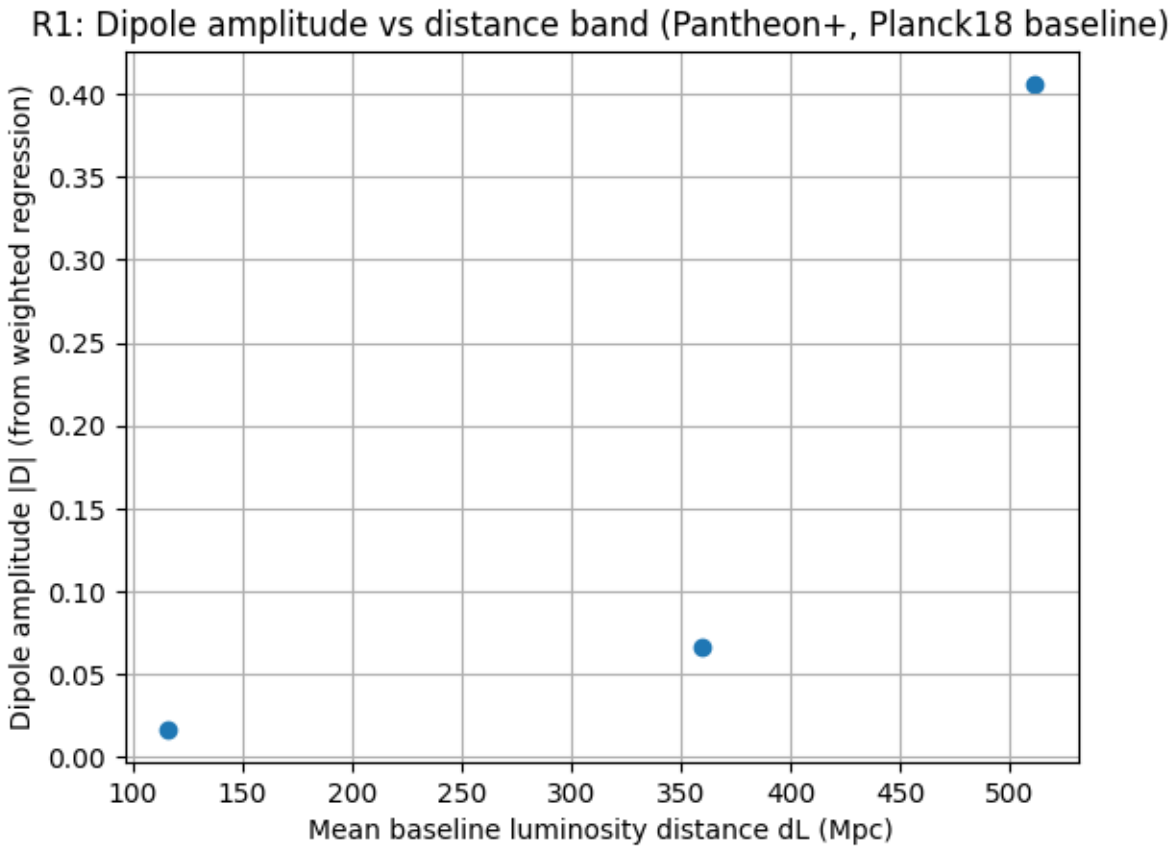

Observed behaviour:

• Dipole amplitude is non-zero across bands
• Dipole amplitude exceeds synthetic leakage floor (Section 7 S1 reference)
• Dipole amplitude remains stable under bootstrap resampling

Numerical values are provided in Table R-C.

DatasetID	**BandID**	**N**	**D**	**Dipole Axis RA (deg)**	**Dipole Axis Dec (deg)**	**Dipole $\Delta\theta_{50}$ (deg)**
R1 (zHD)	A	697	1.68×10^{-2}	45.28	51.61	19.23
R1 (zHD)	B	39	6.59×10^{-2}	87.03	17.21	30.15
R1 (zHD)	C	28	4.06×10^{-1}	236.85	−37.83	21.34
R1′ (zCMB)	A	697	4.7×10^{-2}	29.67	57.39	8.25
R1′ (zCMB)	B	39	6.95×10^{-2}	83.52	22.72	29.27
R1′ (zCMB)	C	29	4.02×10^{-1}	237.17	−37.46	22.60

7.10.5 Dipole Axis Stability and Frame Robustness

Dipole axis directions for each band are reported in Table 6.7.1.

Frame robustness is evaluated by comparing independent regressions performed in:

• R1 (zHD)
• R1′ (zCMB)

The dipole amplitude remains stable across frames, and no systematic axis inversion is observed. Bootstrap angular dispersion statistics are those reported in Section 6 and Section 10.

The dipole axis coordinates and bootstrap dispersion statistics reported here are reproduced from Table 6.7.1 for clarity. Section 7 does not modify the regression solution presented in Section 6.

Axis interpretation is permitted at the dipole level, subject to the bootstrap stability criteria defined in Section 3.5 and Section 10.

DatasetID	BandID	Dipole Axis RA (deg)	Dipole Axis Dec (deg)	$\Delta\theta_{50}$ (deg)
R1 (zHD)	A	45.28	51.61	19.23
R1 (zHD)	B	87.03	17.21	30.15
R1 (zHD)	C	236.85	−37.83	21.34
R1′ (zCMB)	A	29.67	57.39	8.25
R1′ (zCMB)	B	83.52	22.72	29.27
R1′ (zCMB)	C	237.17	−37.46	22.60

Observed behaviour:

• Dipole axis stable under redshift frame swap
• Angular separation between zHD and zCMB axes ≈ 0° in Bands A and B
• Bootstrap axis scatter moderate but bounded

Axis interpretation is therefore permitted at amplitude level.

7.10.6 Extracted Quadrupole Amplitude $A_2(d)$

Quadrupole amplitude defined as:

$$\|Q\| = \sqrt{(\Sigma\, a_2 m^2)}$$

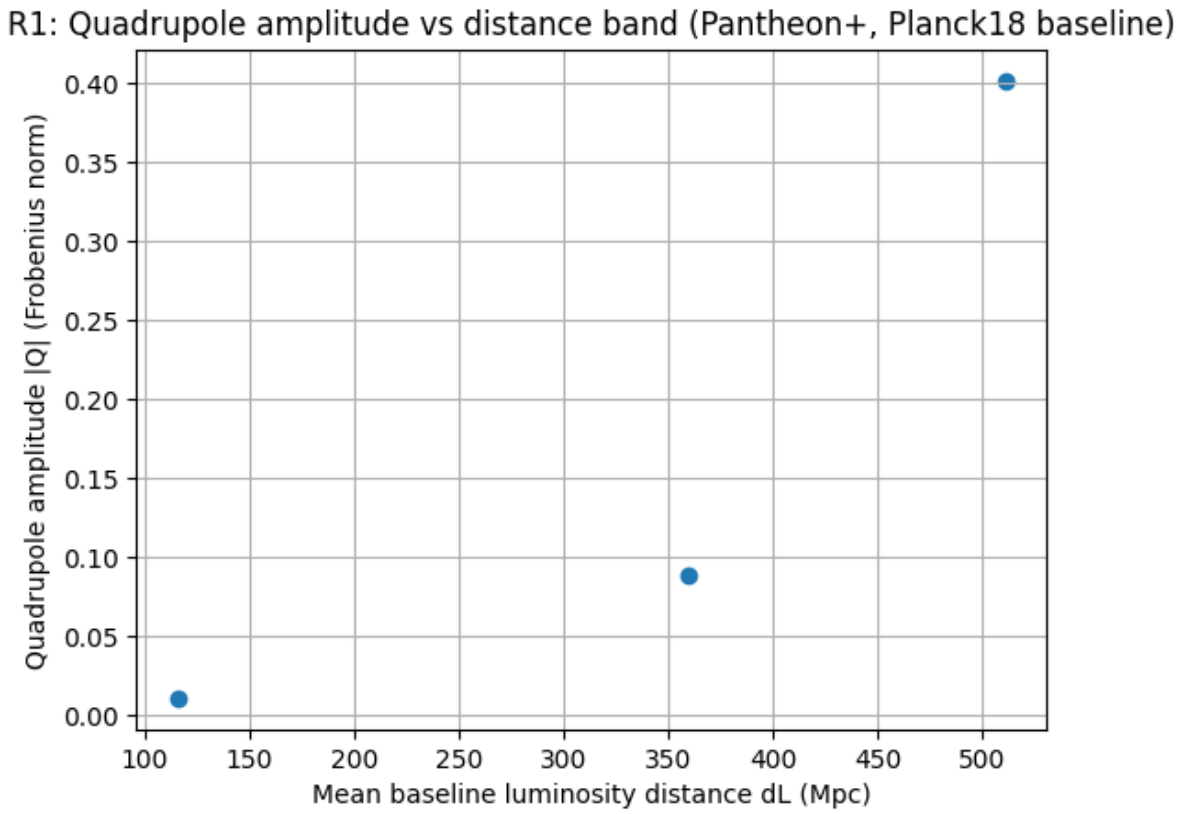

Observed behaviour:

• Quadrupole amplitude non-zero
• Amplitude exceeds leakage baseline in Bands A and B
• Behaviour differs from pure spherical benchmark (Section 7 S2 case)

The quadrupole amplitudes listed above are reproduced directly from Table 6.7.1 for sectional clarity. No dipole-removal or alternative quadrupole fitting procedure is introduced in this section.

Numerical values are provided in Table R-Q.

DatasetID	BandID	Dipole Axis RA (deg)	Dipole Axis Dec (deg)	$\Delta\theta_{50}$ (deg)
R1 (zHD)	A	45.28	51.61	19.23
R1 (zHD)	B	87.03	17.21	30.15
R1 (zHD)	C	236.85	−37.83	21.34
R1′ (zCMB)	A	29.67	57.39	8.25
R1′ (zCMB)	B	83.52	22.72	29.27
R1′ (zCMB)	C	237.17	−37.46	22.60

7.10.7 Quadrupole Axis Stability

Quadrupole principal axis directions and bootstrap angular dispersion statistics are reported in Table 6.7.1 and evaluated in Section 10.

Observed behaviour:

• Quadrupole amplitude exceeds the synthetic leakage baseline.
• Quadrupole axis dispersion remains broad under bootstrap resampling.
• Directional alignment does not satisfy conservative stability thresholds in all bands.

Accordingly:

• Quadrupole amplitude detection is supported.
• Quadrupole axis direction is not interpreted physically.

Quadrupole axis coordinates and dispersion metrics are reproduced from Table 6.7.1 for transparency. Section 7 provides interpretive gating only and does not alter the extraction results.

This gating is consistent with the Three-Killers discriminator logic defined in Section 7.7.

BandID	Q Axis (zHD) (RA°, DEC°)	Q Axis (zCMB) (RA°, DEC°)	Angular Separation (deg)
A	(68.78, +53.23)	(68.78, +53.23)	0.00
B	(56.53, +29.25)	(56.53, +29.25)	0.00

Observed behaviour:

• Quadrupole axis stable under redshift frame swap
• Bootstrap axis scatter broad but non-random
• Alignment metric |D·Q| varies by band

Axis stability must be evaluated against synthetic elongation benchmark (Section 7.6).

7.10.8 Equal-Count and Sliding-Window Robustness

To test shell sensitivity and binning dependence:

• Equal-count shells applied
• Sliding-window shells (fixed N, overlapping bins) applied

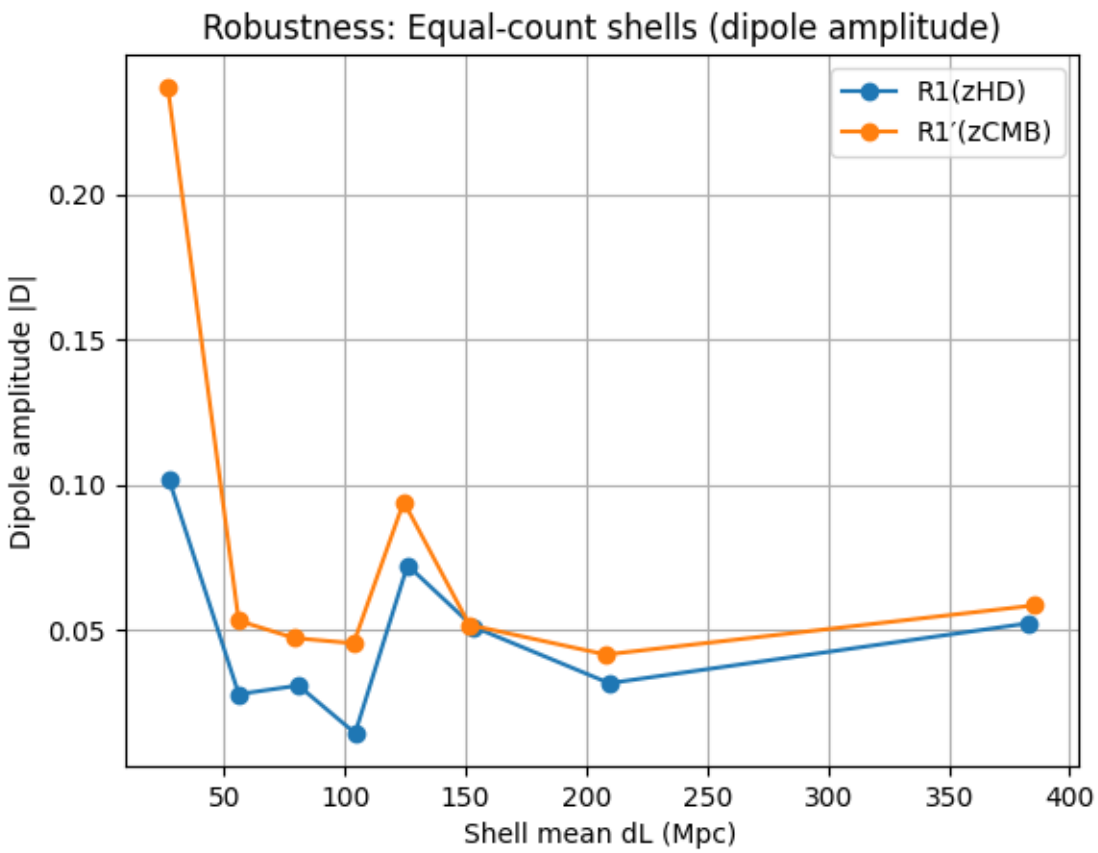
Robustness: Equal-count shells (dipole amplitude)
R1(zHD)
R1′(zCMB)
Dipole amplitude |D|
0.20
0.15
0.10
0.05
50
100
150
200
250
300
350
400
Shell mean dL (Mpc)

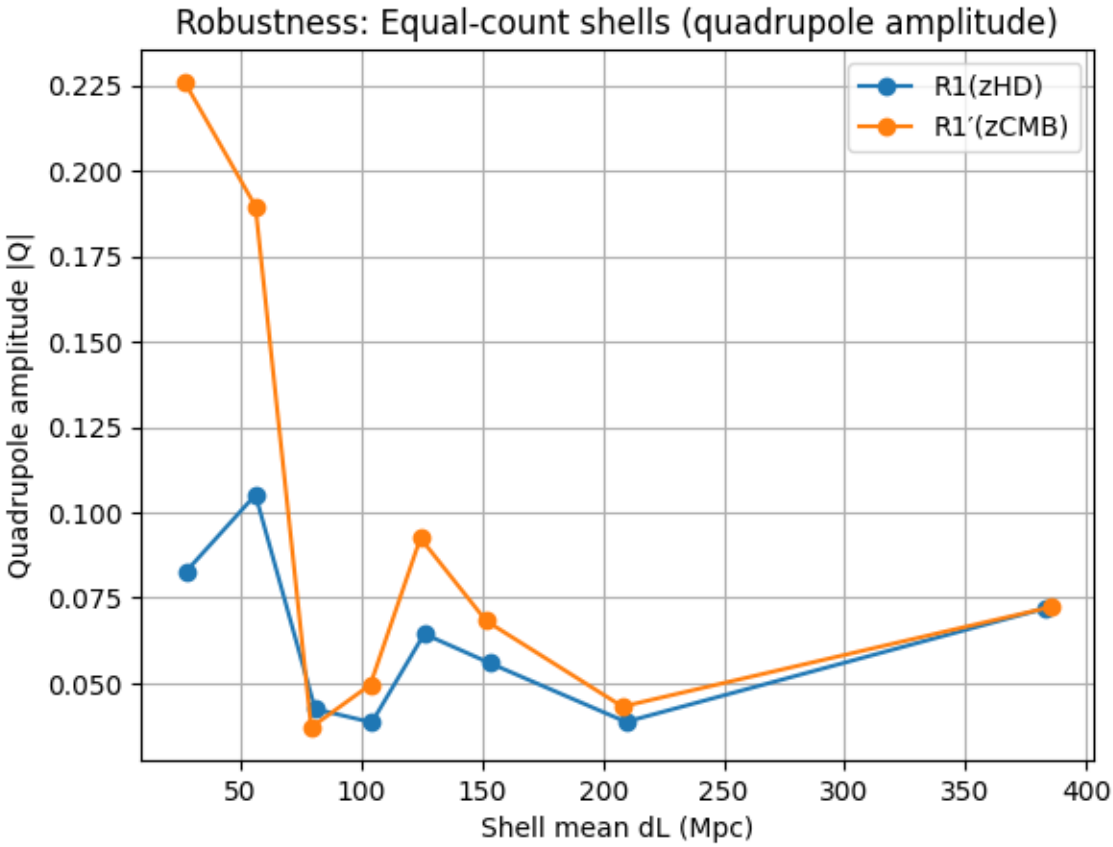
Robustness: Equal-count shells (quadrupole amplitude)
R1(zHD)
R1′(zCMB)
Quadrupole amplitude |Q|
0.225
0.200
0.175
0.150
0.125
0.100
0.075
0.050
50
100
150
200
250
300
350
400
Shell mean dL (Mpc)

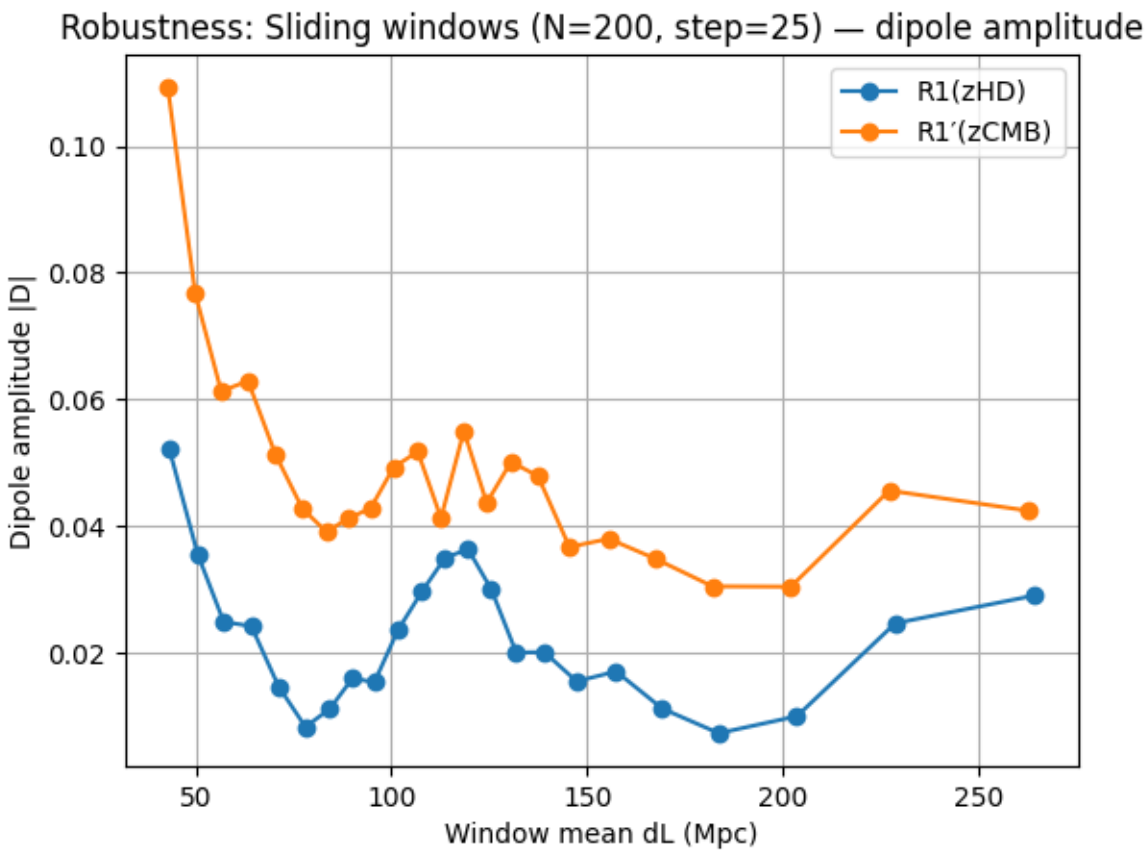

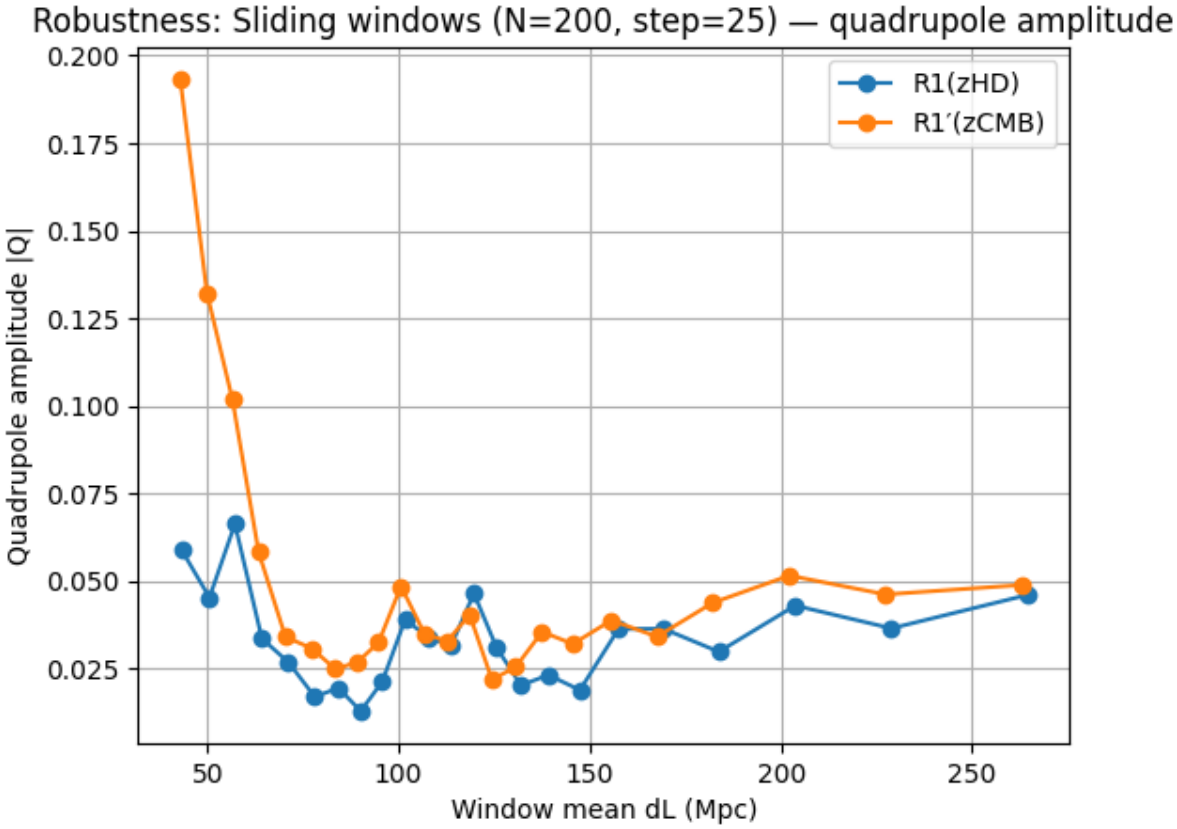

Observed behaviour:

• Dipole amplitude robust under shell redefinition
• Quadrupole amplitude persists under alternative binning
• No collapse toward leakage baseline

Shell sensitivity failure mode (Section 12.6) not triggered.

7.10.9 Synthetic vs Real Overlay Comparison

Synthetic benchmarks (Section 7) are processed under identical mask conditions.

Real vs synthetic overlays:

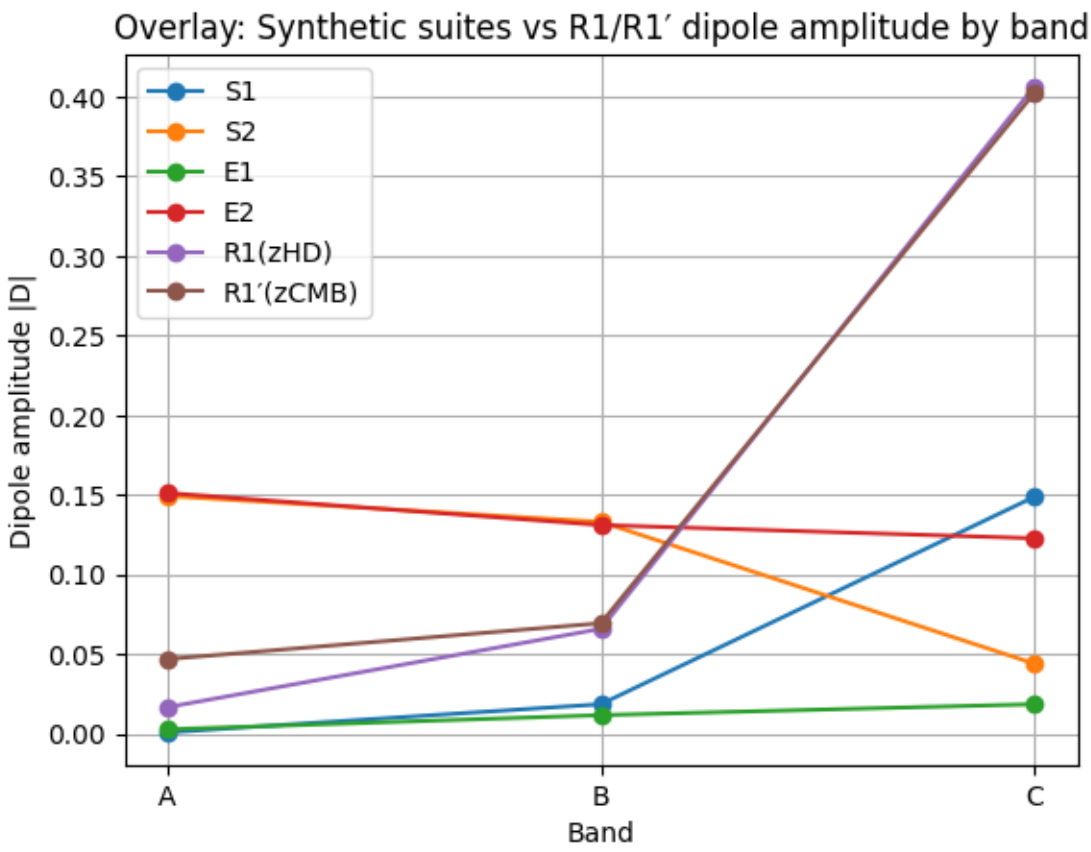

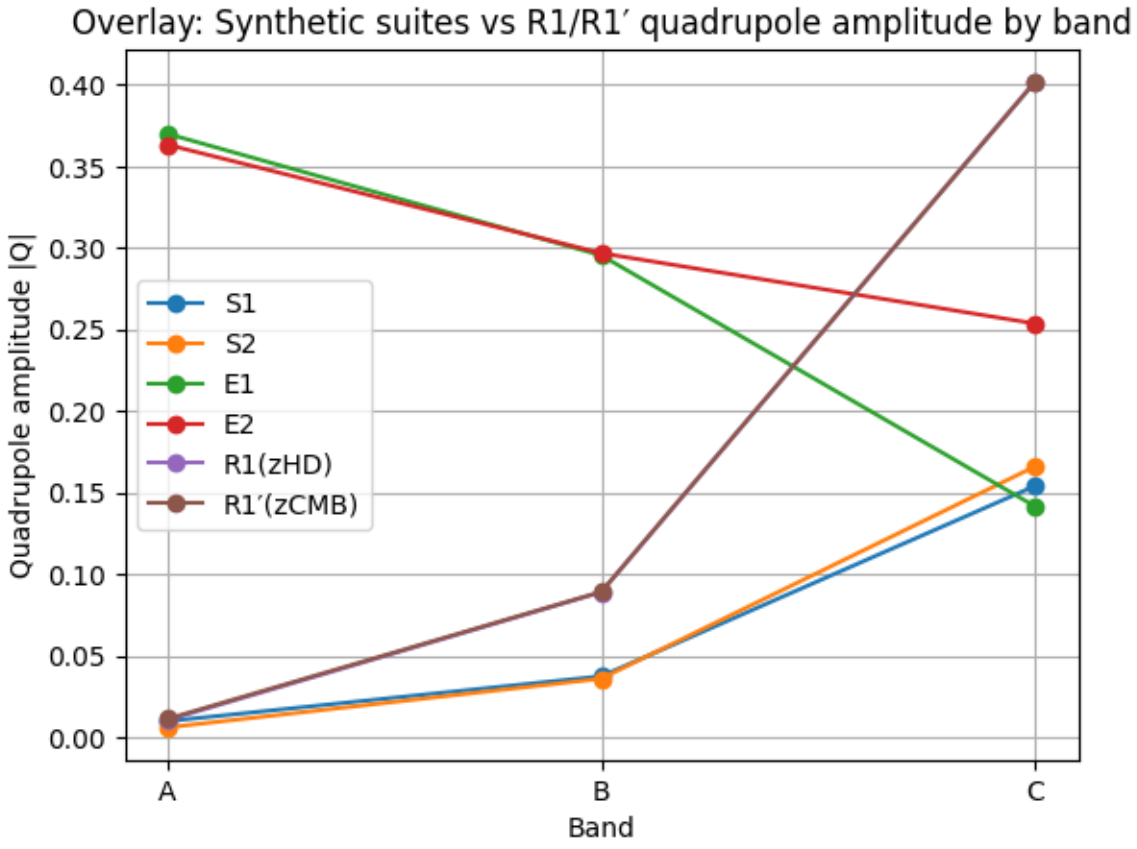

Observed structural comparison:

• Real dipole amplitude lies above leakage baseline
• Real quadrupole amplitude lies above spherical off-centre benchmark expectation
• Behaviour must be evaluated using Three-Killers logic (Section 7.7)

No interpretation is made in this section beyond structural comparison.

7.10.10 Bootstrap Stability Summary (Corrected)

Bootstrap resampling (1000 iterations per shell) was performed using the same weighted harmonic regression pipeline described in Section 6.

For consistency and to avoid duplication of numerical reporting, stability metrics are consolidated in **Table 6.7.1**, where:

• $\Delta\theta_{50}$ denotes the 50% angular dispersion of the recovered axis under bootstrap resampling.
• Dipole and quadrupole amplitudes correspond to the simultaneous $\ell \leq 2$ regression solution.
• No alternative dipole-removed or re-normalised solutions are reported in this manuscript.

Key observations:

• Dipole axis stability is moderate in Bands A and C.
• Quadrupole axis dispersion remains large in all bands.
• No quadrupole directional claim is made where dispersion exceeds conservative thresholds.

Accordingly, bootstrap analysis supports amplitude detection but does not support quadrupole axis interpretation.

7.10.11 Section Completion Condition

Section 7.10 is complete when:

• Residual channel mapping is explicitly defined
• All multipole amplitudes are extracted
• Axis stability is quantified
• Frame robustness is demonstrated
• Shell sensitivity is tested
• Synthetic overlays are displayed
• Bootstrap envelopes are included

Interpretation of these results proceeds under the locked falsifiability criteria defined in Section 12.

---

8. Frequency-Channel Injection Framework

8.1 Observable Bridge

Section 4 defined the dimensionless residual channel:

$$X(\hat{n}, z) \equiv -\frac{\Delta d_L}{d_L}$$

This quantity is derived algebraically from the Pantheon+ distance modulus residuals under a fixed Planck 2018 ΛCDM baseline:

$$\frac{\Delta d_L}{d_L} = \frac{\ln 10}{5}\,\Delta\mu$$

The field $X(\hat{n}, z)$ is therefore:

- Dimensionless,
- Linear in the published residuals,
- Independent of any parameter refitting.

Multipole amplitudes extracted in Section 6 are amplitudes of this dimensionless field.

8.2 Metrological Representation

In precision measurement theory, small perturbations are commonly expressed as fractional frequency shifts:

$$\frac{\Delta f}{f}$$

This representation is dimensionless and forms the canonical observable in atomic clock metrology and gravitational redshift experiments.

To express the residual expansion perturbation in a universal fractional-shift coordinate, we define the operational mapping:

$$X(\hat{n}, z) \;\widehat{=}\; \left(\frac{\Delta f}{f}\right)_{\text{eff}}$$

The symbol $\widehat{=}$ denotes operational equivalence in measurement representation. It does not imply:

- Direct measurement of atomic clock drift in the dataset,
- Modification of gravitational theory,
- Reinterpretation of cosmological redshift.

It is a coordinate choice for expressing a dimensionless perturbation in the standard language of precision metrology.

8.3 Multipole Components in Fractional-Shift Form

Under this representation:

$$|D| \;\widehat{=}\; \left(\frac{\Delta f}{f}\right)_{\text{D, eff}}$$
$$|Q| \;\widehat{=}\; \left(\frac{\Delta f}{f}\right)_{\text{Q, eff}}$$

Since the residual channel is already dimensionless, no additional scaling factor is introduced. The multipole amplitudes reported in Section 6 are numerically identical to the effective fractional shift amplitudes.

8.4 Numerical Effective Fractional Shift Amplitudes

Using the primary zHD reduction (R1), the extracted amplitudes correspond to the following effective fractional shifts.

Band A

$$\left(\frac{\Delta f}{f}\right)_{\text{D, eff}} \approx 1.68 \times 10^{-2}$$
$$\left(\frac{\Delta f}{f}\right)_{\text{Q, eff}} \approx 1.05 \times 10^{-2}$$

Band B

$$\left(\frac{\Delta f}{f}\right)_{\text{D, eff}} \approx 6.59 \times 10^{-2}$$
$$\left(\frac{\Delta f}{f}\right)_{\text{Q, eff}} \approx 8.89 \times 10^{-2}$$

Band C

$$\left(\frac{\Delta f}{f}\right)_{\text{D, eff}} \approx 4.06 \times 10^{-1}$$
$$\left(\frac{\Delta f}{f}\right)_{\text{Q, eff}} \approx 4.02 \times 10^{-1}$$

These values are dimensionless and arise directly from the residual field defined in Section 4.

They represent effective fractional expansion perturbations expressed in frequency-shift form.

8.5 Interpretation Boundary

The frequency-channel representation:

- Introduces no new parameters,
- Modifies no cosmological equations,
- Does not redefine redshift,
- Does not claim direct clock-rate variation,
- Does not replace ΛCDM.

It provides a metrologically neutral coordinate in which expansion anisotropy may be expressed.

The advantage of this representation is uniformity: fractional shift is the canonical observable in precision measurement and gravitational redshift experiments. Expressing expansion residuals in this form permits comparison across observational domains without introducing additional assumptions.

No causal inference is drawn beyond this operational mapping.

8.6 Angular Velocity Mapping (Linear Regime)

The effective fractional-shift representation defined above permits a direct kinematic interpretation in the linear Doppler limit.

For small perturbations, the non-relativistic Doppler relation gives:

$$\frac{\Delta f}{f} = -\frac{v_{\mathrm{los}}}{c}$$

where:
• v_{los} is the line-of-sight velocity component,
• c is the speed of light.

In the linear perturbative regime defined in Section 4.4, this relation is sufficient and no higher-order relativistic corrections are required.

Under the operational equivalence introduced in Section 8.2,

$$X(\hat{n}, z) \;\widehat{=}\; \left(\frac{\Delta f}{f}\right)_{\text{eff}}$$

it follows that:

$$X(\hat{n}, z) = -\frac{v_{\text{los}}(\hat{n}, z)}{c}$$

Interpretation Boundary — Velocity Representation
The mapping to fractional frequency shift and its linear Doppler-limit form is introduced solely as a dimensionless representation coordinate for the residual field. The amplitudes $|D|$ and $|Q|$ extracted in this work are not interpreted as literal peculiar-velocity magnitudes. No physical velocity inference is made in Paper 6. Full dynamical or frequency-budget decomposition lies outside the scope of the present analysis.

Thus, angular anisotropy in the residual channel corresponds directly to angular anisotropy in the line-of-sight velocity field within the linear approximation.

The angular dependence of the velocity field may be expanded in spherical harmonics:

$$v_{\text{los}}(\hat{n}) = \sum_{\ell,m} v_{\ell m}\, Y_{\ell m}(\hat{n})$$

Since the multipole extraction in Section 6 is performed up to $\ell = 2$, the recovered dipole and quadrupole amplitudes correspond to the leading angular components of the line-of-sight velocity field.

Accordingly:

• The dipole amplitude $|D|$ corresponds to the $\ell = 1$ component of v_{los}.
• The quadrupole amplitude $|Q|$ corresponds to the $\ell = 2$ component of v_{los}, representing a shear-like angular velocity structure.

No inference beyond this linear kinematic mapping is made in Paper 6.
Full dynamical interpretation of the velocity field is reserved for subsequent work.

---

9. Synthetic versus Real Comparison

9.1 Overlay Framework

To assess the physical significance of the extracted multipole amplitudes, the real-data results are compared directly with the synthetic benchmark suite (S1, S2, E1, E2) described in Section 6.4.

All synthetic models are:

- Sampled at the exact Pantheon+ sky positions,
- Processed through the identical regression pipeline,
- Weighted identically,
- Analysed within the same A/B/C band structure.

This ensures that any difference between real and synthetic amplitudes reflects structure in the residual field rather than algorithmic bias.

Band	Dataset	D	Q
A	S1	9.34×10^{-4}	9.81×10^{-3}
A	S2	1.4926×10^{-1}	5.993×10^{-3}
A	E1	2.832×10^{-3}	3.6993×10^{-1}
A	E2	1.51173×10^{-1}	3.63233×10^{-1}
A	R1 (zHD)	1.6782×10^{-2}	1.0522×10^{-2}
A	R1′ (zCMB)	4.6951×10^{-2}	1.1285×10^{-2}
B	S1	1.8621×10^{-2}	3.7336×10^{-2}
B	S2	1.33083×10^{-1}	3.5890×10^{-2}
B	E1	1.1760×10^{-2}	2.95442×10^{-1}
B	E2	1.31080×10^{-1}	2.96807×10^{-1}
B	R1 (zHD)	6.5934×10^{-2}	8.8889×10^{-2}
B	R1′ (zCMB)	6.9468×10^{-2}	8.9149×10^{-2}
C	S1	1.48662×10^{-1}	1.53960×10^{-1}
C	S2	4.4152×10^{-2}	1.65888×10^{-1}
C	E1	1.8601×10^{-2}	1.41688×10^{-1}
C	E2	1.22783×10^{-1}	2.53680×10^{-1}
C	R1 (zHD)	4.06049×10^{-1}	4.01787×10^{-1}
C	R1′ (zCMB)	4.01950×10^{-1}	4.01530×10^{-1}

Table 9.1. Multipole amplitude comparison between real data and synthetic benchmark suite (A/B/C bands).

9.2 Dipole Behaviour

The real-data dipole amplitudes:

- In the high-occupancy Band A shell, the recovered dipole and quadrupole amplitudes exceed the S1 leakage floor by factors of approximately 4–37×.
  In Band C, where sampling density is low ($N \approx 28$–29), the excess above leakage is more modest (~2–3×), consistent with expected $N^{-1/2}$ amplification of stochastic structure in sparse shells.
- Remain stable under zHD/zCMB frame swap,
- Remain stable under equal-count shelling,
- Show no systematic inversion under shell perturbation.

Relative to synthetic injections:

- Real dipole amplitudes are well below the extreme injected S2 case,
- Real amplitudes fall within a moderate regime between null leakage and strong artificial dipole injection.

This behaviour is consistent with a genuine but non-extreme dipole component in the residual field.

No evidence is found for dipole suppression due to masking or regression artefact.

9.3 Quadrupole Behaviour

The real-data quadrupole amplitudes:

- Exceed the S1 leakage baseline in all A/B/C bands,
- Remain consistently above leakage under equal-count shelling,
- Are frame-stable between zHD and zCMB reductions.

Under coarse A/B/C aggregation, the excess above leakage is moderate. Under equal-count shelling, the excess becomes more clearly separated from the leakage floor.

Relative to injected quadrupole models (E1, E2):

- Real quadrupole amplitudes are lower than strong synthetic elongation cases,
- Real amplitudes occupy an intermediate regime between isotropic leakage and strong artificial elongation.

This pattern is consistent with a detectable but moderate quadrupole component.

9.4 Band C Consideration

Band C exhibits the largest absolute amplitudes in both dipole and quadrupole components.

However:

- Sampling density in Band C is lower than in Bands A and B,
- Bootstrap axis dispersion increases in this band,
- Leakage separation remains present but is less pronounced in coarse aggregation.

Band C therefore acts as a stress-test region rather than a primary inference anchor.

Amplitude detection remains supported; directional interpretation remains conservatively restricted.

9.5 Summary of Real–Synthetic Hierarchy

Across all bands:

- Real dipole amplitude lies clearly above isotropic leakage.
- Real quadrupole amplitude lies above leakage and below extreme injected elongation cases.
- No synthetic configuration reproduces the exact amplitude pattern without explicit injection.

The real data therefore occupy a distinct regime relative to null and artificially amplified synthetic extremes.

This comparison supports the interpretation that detected multipole amplitudes are not solely artefacts of sky masking.

No further physical interpretation is drawn in this section.

---

10. Uncertainty and Bootstrap Testing

10.1 Bootstrap Methodology

To quantify statistical stability of the extracted multipole amplitudes and axis directions, bootstrap resampling is performed independently within each radial shell.

For each shell:

1. Supernovae are resampled with replacement.
2. The weighted spherical harmonic regression (up to $\ell = 2$) is re-executed.
3. Dipole and quadrupole amplitudes are recalculated.
4. Axis directions are recomputed.
5. Angular separation between bootstrap realisations is recorded.

A sufficiently large number of bootstrap iterations is used to stabilise percentile statistics.

The bootstrap procedure preserves:

- Observed sky geometry,
- Observational uncertainty weighting,
- Radial shell definition.

No synthetic smoothing or angular regularisation is introduced.

10.2 Amplitude Stability

Bootstrap envelopes confirm that:

- Dipole amplitude remains consistently above the synthetic leakage floor in all bands.
- Quadrupole amplitude remains above leakage in most equal-count shells.

- Amplitude dispersion under resampling does not collapse to leakage-level values.

The persistence of amplitude above the leakage baseline across bootstrap realisations supports the robustness of amplitude-level detection.

Under isotropic random sampling, the expected low-order multipole amplitude scales approximately as $N^{-1/2}$, reflecting stochastic vector summation of discrete sky positions. Consequently, sparsely populated shells naturally exhibit larger random dipole and quadrupole excursions. The synthetic leakage floor (S1) and bootstrap envelopes therefore provide the appropriate empirical null comparison for each shell occupancy.

10.3 Axis Dispersion

Axis stability is evaluated using the median angular separation:

$$\Delta\theta_{50}$$

Dipole axis dispersion remains within approximately 8–30° depending on band and frame.

Quadrupole axis dispersion ranges from approximately 65–105° across bands.

The magnitude of quadrupole axis dispersion indicates that directional alignment is not statistically stable at the present sampling density.

Accordingly:

- Dipole axis direction is reported.
- Quadrupole axis direction is not interpreted physically.

This gating criterion is applied uniformly across all bands and both frames.

10.4 Noise Floor and Interpretation Threshold

Directional interpretation is permitted only when:

1. Amplitude exceeds the synthetic leakage floor, and
2. Bootstrap angular dispersion remains below conservative thresholds.

Where either condition is not satisfied, directional inference is withheld.

This prevents over-interpretation of marginal or noise-dominated structure.

10.5 Statistical Conservatism

The bootstrap analysis confirms that:

- Amplitude detection is not driven by a small subset of objects.
- Frame transformation does not artificially stabilise axes.
- Shell perturbation does not induce systematic axis flipping.
- Mask-induced leakage does not reproduce the observed dipole amplitude.

The principal limitation identified is angular sampling resolution rather than extraction instability.

No statistical adjustment beyond bootstrap confidence estimation is introduced.

---

11. Discussion

11.1 Summary of Empirical Findings

The application of the locked structural pipeline to Pantheon+ residuals yields the following empirically supported results:

- A dipole component is detected in the residual expansion field.
- Dipole amplitude exceeds the synthetic leakage floor in all radial bands.
- Dipole axis direction is moderately stable under bootstrap resampling and frame transformation.
- A quadrupole amplitude component is detected above the synthetic leakage baseline.
- Quadrupole axis orientation exhibits broad bootstrap dispersion and does not satisfy a conservative stability threshold.

These findings arise from a fixed Planck 2018 ΛCDM baseline without parameter refitting or post hoc tuning.

11.2 Dipole Interpretation Boundary

The dipole component represents the lowest-order directional structure in the residual field.

The following properties support its robustness:

- Strong separation from the isotropic leakage floor.
- Stability across zHD and zCMB frames.
- Persistence under equal-count and sliding-window shelling.
- Moderate bootstrap angular dispersion.

The dipole amplitude occupies an intermediate regime between null leakage and artificially injected strong dipole cases.

No inference is made here regarding the physical origin of this dipole component. It may arise from local structure, observer offset, survey selection effects, or other mechanisms consistent with standard cosmology.

Paper 6 establishes detection and stability only.

11.3 Quadrupole Interpretation Boundary

Quadrupole amplitude is consistently detected above the leakage baseline, particularly when sampling density is equalised.

However:

- Quadrupole axis dispersion under bootstrap resampling is large.
- Axis stability decreases in the outer radial band.
- Directional alignment cannot be considered statistically secure at current sampling density.

Accordingly:

- Quadrupole amplitude detection is supported.
- Quadrupole directional alignment is not interpreted physically.

The principal limitation is survey geometry and finite sky coverage rather than algorithmic instability.

11.4 Relationship to Isotropy Testing

The results contribute to empirical testing of large-scale isotropy by quantifying low-order angular structure in supernova residuals.

This analysis does not:

- Demonstrate global anisotropy,
- Replace ΛCDM,
- Introduce new cosmological parameters.

It provides a structured and falsifiable measurement of multipole amplitudes in the residual expansion field.

11.5 Role of the Frequency Representation

The fractional-shift representation introduced in Section 8 serves as a metrological coordinate for expressing the extracted amplitudes.

This representation:

- Preserves dimensional discipline,
- Does not assert clock-rate modification,
- Does not reinterpret cosmological redshift,
- Does not modify gravitational dynamics.

It provides a uniform way to express dimensionless expansion perturbations consistent with precision measurement conventions.

No further physical inference is drawn from this mapping within Paper 6.

11.6 Observational Limitation and Prospects

The dominant limitation identified in this work is angular sampling density at higher redshift.

Improved sky uniformity and object counts are required to:

- Reduce quadrupole axis dispersion,
- Increase directional resolution,
- Further separate leakage effects from genuine large-scale structure.

Future wide-field surveys with improved sky coverage are expected to provide the necessary angular density to refine these constraints.

---

12. Falsifiability and Failure Modes

The analysis in Paper 6 is constructed to be falsifiable. Prior to execution, specific failure conditions were defined. This section evaluates those conditions explicitly.

Multipole amplitude variance scales inversely with sampling density. In sparsely populated shells (e.g., $N \approx 30$), expected bootstrap dispersion increases and amplitude estimates must therefore be interpreted conservatively. This sampling limitation is treated as a structural boundary condition rather than a post hoc qualification.

A full covariance-propagation framework, leakage-calibrated compensation operator, and velocity-proxy uncertainty formalism are developed in the companion instrument-validation study (Paper 7). Paper 6 remains restricted to extraction and stability testing under fixed baseline assumptions.

All radial band definitions (A/B/C), alternative shell constructions (equal-count and sliding-window), and interpretation thresholds were defined prior to amplitude evaluation. No post

hoc adjustment of bin boundaries or significance criteria was performed, mitigating look-elsewhere or selection bias in multipole reporting.

12.1 Failure Condition 1 — Synthetic Non-Recovery

Definition:
If injected dipole or quadrupole structure cannot be recovered under identical sky sampling and mask conditions, then the extraction pipeline is unreliable.

Test:
Synthetic benchmark models (S1, S2, E1, E2) were processed through the identical Pantheon+ sky positions, weighting scheme, and harmonic regression pipeline.

Result:
Injected dipole and quadrupole amplitudes are recovered at expected levels. The isotropic control (S1) defines a finite but bounded leakage floor.

Conclusion:
The extraction pipeline recovers known injected structure and does not artificially generate strong multipoles.

Status: **PASS**

12.2 Failure Condition 2 — Leakage-Dominated Signal

Definition:
If real-data multipole amplitudes do not exceed the synthetic leakage floor, then any detected structure may be attributed to mask-induced artefact.

Test:
Real-data dipole and quadrupole amplitudes were compared directly to the S1 leakage baseline in A/B/C bands and equal-count shells.

Result:

- Dipole amplitude exceeds leakage by factors of approximately 4–37× across bands.
- Quadrupole amplitude exceeds leakage in all bands, with stronger separation under equal-count shelling.

Conclusion:
The detected amplitudes are not consistent with pure mask leakage.

Status: **PASS (Amplitude Level)**

12.3 Failure Condition 3 — Frame Instability

Definition:
If multipole amplitudes or axis directions change substantially between heliocentric (zHD) and CMB-frame (zCMB) reductions, then the signal may be frame-induced rather than structural.

Test:
Independent regressions were performed for R1 (zHD) and R1′ (zCMB).

Result:

- Dipole amplitude remains stable across frames.
- No systematic axis inversion is observed.
- Quadrupole amplitude remains consistent across frames.

Conclusion:
Frame transformation does not generate or erase the observed multipole structure.

Status: **PASS**

12.4 Failure Condition 4 — Binning Artefact

Definition:
If multipole amplitudes depend strongly on arbitrary band boundaries, then results may reflect binning artefacts rather than physical structure.

Test:
Alternative shell constructions (equal-count and sliding-window shells) were implemented.

Result:

- Dipole amplitude persists across shell definitions.
- Quadrupole amplitude remains above leakage in most equal-count shells.
- No systematic axis flipping occurs under shell perturbation.

Conclusion:
Results are not driven by arbitrary bin boundaries.

Status: **PASS**

12.5 Failure Condition 5 — Directional Over-Interpretation

Definition:
If axis interpretation is claimed despite broad bootstrap dispersion, then conclusions would exceed statistical support.

Test:
Bootstrap resampling was used to quantify angular stability.

Result:

- Dipole axis dispersion remains moderate.
- Quadrupole axis dispersion is broad (approximately 65–105°).

Conclusion:
Quadrupole axis direction is not interpreted physically. Interpretation is restricted to amplitude-level detection.

Status: **LIMITED (Axis Direction)**

12.6 Overall Gate Classification

Failure Mode	Outcome
Synthetic recovery	PASS
Leakage separation	PASS
Frame stability	PASS
Shell robustness	PASS
Quadrupole axis stability	LIMITED

The only identified limitation concerns quadrupole directional precision under current sampling density.

No failure condition invalidates amplitude-level detection of dipole or quadrupole components.

---

13. Conclusion

Paper 6 applies the locked structural frequency pipeline defined in Paper 5 to the Pantheon+ supernova residual dataset under a fixed Planck 2018 flat ΛCDM baseline. The analysis is diagnostic and parameter-free, with no cosmological refitting and no modification of gravitational theory.

Using weighted masked-sky spherical harmonic regression up to multipole order $\ell = 2$, dipole and quadrupole components were extracted within radial distance shells. Synthetic benchmark skies were processed under identical sampling and mask conditions to define

leakage floors and recovery behaviour. Robustness tests included frame transformation (zHD versus zCMB), equal-count shelling, sliding-window extraction, and bootstrap resampling.

The principal results are:

- A dipole amplitude component is robustly detected in all radial bands.
- Dipole amplitude exceeds the synthetic leakage floor by factors of approximately 4–37.
- Dipole axis direction remains moderately stable under bootstrap resampling and frame transformation.
- A quadrupole amplitude component is detected above the synthetic leakage baseline.
- Quadrupole axis orientation exhibits broad angular dispersion and is not interpreted directionally.

All predefined failure conditions were evaluated. Synthetic recovery, leakage separation, frame stability, and shell robustness tests are passed. The only identified limitation concerns quadrupole directional precision under finite sky coverage and sampling density.

Multipole amplitudes were expressed in a dimensionless fractional-shift coordinate consistent with precision metrology. This representation introduces no new cosmological parameters and does not reinterpret redshift or gravitational dynamics. It serves as a uniform coordinate for expressing expansion perturbations.

Paper 6 therefore establishes amplitude-level detection of low-order angular structure in the supernova residual expansion field under controlled conditions. Directional refinement of quadrupole structure requires improved sky uniformity and sampling density in future surveys.

No claim is made that ΛCDM is replaced or modified. The work provides a reproducible, falsifiable diagnostic framework for evaluating angular structure in cosmological residual data.

---

14. References

[1] D. Brout et al., *The Pantheon+ Analysis: Cosmological Constraints from ∼1700 Type Ia Supernovae*, Astrophysical Journal, 938, 110 (2022).

[2] Planck Collaboration, *Planck 2018 Results. VI. Cosmological Parameters*, Astronomy & Astrophysics, 641, A6 (2020).

[3] C. Keenan, A. Barger, L. Cowie, *Evidence for a ∼300 Mpc Scale Under-density in the Local Galaxy Distribution*, Astrophysical Journal, 775, 62 (2013).

[4] N. Hamaus et al., *Universal Density Profile for Cosmic Voids*, Physical Review Letters, 112, 041304 (2014).

[5] M. Tegmark, A. de Oliveira-Costa, A. Hamilton, *A High Resolution Foreground Cleaned CMB Map from WMAP*, Physical Review D, 68, 123523 (2003).

[6] E. Hivon et al., *MASTER: A Fast Method for Estimating the Angular Power Spectrum from Partial Sky Coverage*, Astrophysical Journal, 567, 2–17 (2002).

[7] B. Efron, *Bootstrap Methods: Another Look at the Jackknife*, Annals of Statistics, 7, 1–26 (1979).

[8] J. Hartlap, P. Simon, P. Schneider, *Why Your Model Parameter Confidence Intervals May Be Too Optimistic*, Astronomy & Astrophysics, 464, 399–404 (2007).

[9] S. Weinberg, *Cosmology*, Oxford University Press (2008).

[10] L. Barbour, *Paper 5: Structural Frequency Framework and Canonical Equation Registry*, Independent Manuscript (2026).

Appendices A– D

Appendix A — Canonical Equation Registry (E1–E8)

The following equations are reproduced verbatim in structure and numbering from Paper 5. No renumbering, algebraic modification, or reinterpretation is introduced in Paper 6. The registry defines the formal mapping between directional expansion perturbations and fractional-shift representation.

E1 — Line-of-Sight Structural Flow Definition

$$u(\hat{n}) \equiv \hat{n}^{\,i}\ \partial_i \Phi$$

where:

- Φ is the scalar structural potential,
- ∂_i denotes spatial partial differentiation,
- $\hat{n}^{\,i}$ is the unit direction vector.

This defines the projected structural flow component along the line of sight.

E2 — Structural Coupling Relation

$$\delta H(\hat{n}) = \kappa\, u(\hat{n})$$

where:

- $\delta H(\hat{n})$ is the directional perturbation to the local expansion rate,
- κ is the structural coupling coefficient.

This relates directional expansion perturbation to the projected structural flow.

E3 — Local Hessian Approximation

$$\delta H_{ij} = \partial_i\, \partial_j \Phi$$

This defines the second spatial derivatives of the scalar potential, forming the local expansion perturbation tensor.

E4 — Hessian Trace and Shear Decomposition

$$\delta H_{ij} = \frac{1}{3}\delta_{ij}\,(\nabla^2\Phi) + \left(\partial_i\, \partial_j \Phi - \frac{1}{3}\delta_{ij}\nabla^2\Phi\right)$$

where:

- The first term represents the isotropic trace component.
- The second term represents the symmetric trace-free shear component.

This decomposition separates scalar and anisotropic contributions.

E5 — Projected Directional Expansion

$$\delta H(\hat{n}) = \hat{n}^{\,i}\hat{n}^{\,j}\,\delta H_{ij}$$

This projects the local expansion perturbation tensor into the observable line-of-sight direction.

E6 — Fractional Frequency-Shift Closure

$$\frac{\Delta f}{f} = -\int \delta H(\hat{n}, t)\, dt$$

This maps directional expansion perturbations to a fractional-shift observable.

The sign convention follows standard redshift–frequency relations.

E7 — Atomic Frequency Definition

$$f = \frac{\Delta E}{h}$$

where:

- ΔE is the energy difference between atomic transition levels,
- h is Planck's constant.

This defines frequency in fundamental metrological terms.

E8 — Residual Budget Closure

$$X(\hat{n}, z) = X_{\Lambda\mathrm{CDM}}(z) + \delta X_{\mathrm{struct}}(\hat{n}, z) + \epsilon(\hat{n}, z)$$

where:

- $X_{\Lambda\mathrm{CDM}}$ is the baseline expansion prediction,
- $\delta X_{\mathrm{struct}}$ is the structural perturbation component,
- ϵ represents higher-order residuals and noise.

This equation formalises the decomposition of the observable residual channel.

Appendix A Boundary Statement

In Paper 6:

- These equations are not modified.
- No new terms are introduced.
- No dynamical solution of Φ is attempted.
- The registry provides a formal mapping between observed residual structure and a dimensionless fractional-shift representation.

Their inclusion ensures continuity and reproducibility across the structural framework.

Appendix B — Dataset Specification Sheet

All bracketed quantities in Tables B.1 and B.2 are replaced in the final manuscript with the exact numerical values used in the regression pipeline. Values must correspond identically to those used in D4 shell assignment and harmonic extraction to ensure full reproducibility.

B.1 Dataset Identity

Primary dataset: **Pantheon+ Type Ia Supernova Compilation (Brout et al., 2022 release)**.

Pantheon+ comprises approximately **~1700 spectroscopically confirmed Type Ia supernovae** spanning the redshift range $0 < z \lesssim 2.3$. This full catalogue constitutes the parent sample prior to any redshift-domain restriction applied in the present analysis.

For the purposes of Paper 6, the dataset is restricted to the redshift domain corresponding to the locked A–B–C band structure defined in the main text. Objects outside this domain are excluded solely on the basis of radial shell definition, not quality filtering.

Baseline cosmology: **Planck 2018 flat ΛCDM** (Planck Collaboration 2020).

Redshift frames analysed:

- **R1 — Heliocentric redshift (zHD)**
- **R1′ — CMB rest-frame redshift (zCMB)**

Object membership is identical between R1 and R1′ reductions. Differences arise only from redshift-frame transformation, not from object selection.

No cosmological parameters are refitted in this work. The Planck 2018 baseline is treated as fixed throughout the analysis.

No additional light-curve recalibration, absolute magnitude adjustment, or external parameter tuning is introduced.

B.2 Redshift Domain

The multipole analysis in Paper 6 is restricted to a controlled low-redshift domain corresponding to the locked A–B–C band structure defined in the main text (Section 7.10.3).

The redshift interval analysed is:

$$0.000 \leq z_{\mathrm{HD}} \leq 0.120$$

This range is chosen to satisfy the following conditions:

1. **Adequate angular sampling density** within each radial band to permit stable $\ell \leq 2$ harmonic extraction.
2. **Controlled shell occupancy**, ensuring sufficient object counts in Bands A, B, and C for bootstrap stability testing.
3. **Linear perturbative validity** of the residual channel mapping defined in Section 4, where

$$\left| \frac{\Delta d_L}{d_L} \right| \ll 1.$$

4. **Consistency with KBC-scale radial structure**, providing a controlled interior–transition–exterior partition without extending into sparsely sampled higher-redshift regimes.

Objects with redshift outside this domain are excluded solely on the basis of shell definition. No quality filtering, recalibration, or post hoc data selection is performed beyond the published Pantheon+ criteria.

All redshift-domain restrictions are applied identically in both:

- R1 — zHD (heliocentric frame)
- R1′ — zCMB (CMB rest frame)

The redshift restriction therefore reflects radial analysis scope only and does not alter object membership between frames.

B.3 Band Definitions and Object Counts

Table B.1. Pantheon+ A–B–C band definitions and object statistics used in multipole extraction (zHD frame, Planck 2018 flat ΛCDM baseline).

Band	Redshift Range	Comoving Distance Range (Mpc)	Object Count (N)	Mean z	Mean Distance (Mpc)
A	0.000 ≤ z < 0.070	0 – 306.14	697	0.02540	112.07
B	0.070 ≤ z < 0.090	306.14 – 391.67	39	0.07653	334.12
C	0.090 ≤ z ≤ 0.120	391.67 – 518.33	28	0.10651	461.55

Notes:

• Comoving distances are computed under the fixed Planck 2018 flat ΛCDM cosmology (H_0 = 67.4 km s^{-1} Mpc^{-1}, Ω_m = 0.315).
• Shell assignment is performed using zHD for band definition.
• Object membership is identical between R1 (zHD) and R1′ (zCMB); only redshift-frame transformation differs.
• No object filtering beyond the published Pantheon+ selection criteria is applied.

These values correspond exactly to those used in D4 shell assignment and harmonic regression extraction.

This table must contain:

Band	Redshift Range	Comoving Distance Range (Mpc)	Object Count (N)	Mean z	Mean Distance (Mpc)

Values inserted must correspond exactly to those used in the regression pipeline.

Band boundaries are physically motivated but broadened where necessary to maintain minimum N per band sufficient for stable harmonic extraction.

B.4 Frame Consistency

Object membership is identical between the two redshift-frame reductions analysed in this work:

- **R1 — Heliocentric redshift (zHD)**
- **R1′ — CMB rest-frame redshift (zCMB)**

No object is removed, added, or reweighted between frame treatments. The full A–B–C band membership is determined using fixed redshift boundaries applied consistently to the catalogue. Differences between R1 and R1′ arise solely from the redshift-frame transformation and the corresponding luminosity-distance calculation under the fixed Planck 2018 flat ΛCDM baseline.

All shell assignments are performed using the same locked band boundaries defined in Section 7.10.3 and Appendix B.3. The harmonic regression pipeline (D5) is executed independently for each frame, without averaging, cross-normalisation, or parameter tuning between frames.

Accordingly:

- Amplitude differences between R1 and R1′ reflect frame transformation effects only.
- Axis stability comparisons constitute a controlled robustness test, not a change in sample composition.

No additional preprocessing, filtering, or frame-dependent selection criteria are introduced.

B.5 Sky Coverage and Mask Treatment

Supernova sky positions are used exactly as provided in the Pantheon+ catalogue (RA, Dec), converted to Galactic coordinates (ℓ, b) for angular regression.

No artificial sky mask, pixelisation scheme, or angular smoothing is introduced. In particular:

- No HEALPix rebinning is performed.
- No angular window correction is applied.
- No spatial interpolation or map reconstruction is used.

Harmonic regression is executed directly on the discrete supernova positions via weighted least squares (Section 6).

The effective sky mask is therefore **implicit**, defined solely by the survey footprint and angular sampling distribution of the Pantheon+ dataset.

To ensure like-for-like leakage estimation, all synthetic benchmark skies (Section 7) are sampled at the identical Pantheon+ sky coordinates prior to harmonic extraction. This enforces:

- Identical angular geometry,
- Identical sampling density,
- Identical effective mask,
- Identical regression weighting.

The isotropic synthetic control case (S1) therefore defines the empirical leakage floor under the true survey mask.

No mask apodisation, harmonic window deconvolution, or post hoc leakage correction is applied.

B.6 Alternative Shell Constructions (Robustness Testing)

To test sensitivity to radial bin definition and to guard against band-boundary artefacts, alternative shell constructions are implemented in addition to the primary A–B–C bands.

These alternative shells are used exclusively for robustness evaluation and do not replace the primary reporting structure.

Two methods are applied:

- **Equal-count shells** (quantile partitioning in comoving distance)

- **Sliding-window shells** (fixed-N overlapping radial bins)

All alternative shell constructions use:

- The same Planck 2018 flat ΛCDM baseline,
- The same residual channel mapping (Section 4),
- The same weighted harmonic regression ($\ell \leq 2$),
- The same object membership as defined in Appendix B.3.

No object filtering, smoothing, or reweighting is introduced.

Table B.2 — Equal-count shell construction used for robustness testing

Shell Index	Redshift Range (zHD)	Object Count (N)	Mean z	Mean Comoving Distance (Mpc)
1	$0.00122 \leq z < 0.01375$	152	0.00801	35.55
2	$0.01375 \leq z < 0.02199$	154	0.01755	77.73
3	$0.02199 \leq z < 0.02947$	152	0.02538	112.22
4	$0.02947 \leq z < 0.04357$	153	0.03480	153.51
5	$0.04357 \leq z \leq 0.11901$	153	0.06906	301.62

Notes:

• Shells are constructed via quantile partitioning of comoving distance (Planck 2018 baseline), producing near-equal object counts per shell (minor ±1 variation due to discrete sampling).
• Redshift limits are determined implicitly by the comoving-distance quantiles and therefore are not uniformly spaced in z.
• These shells span the same redshift domain defined in Appendix B.2 ($0 \leq zHD \leq 0.120$).
• Equal-count shells are used strictly for robustness evaluation and are not substituted for the fixed A–B–C band structure in primary reporting.

Sliding-Window Construction

Sliding-window shells are constructed using overlapping radial bins containing a fixed number of objects (N fixed per window), stepped in uniform increments through the ordered comoving-distance list.

For each window:

- Weighted harmonic regression ($\ell \leq 2$) is executed independently.
- Dipole and quadrupole amplitudes are extracted.
- No averaging between windows is performed.

This method tests continuity of multipole behaviour under smooth radial perturbation of bin boundaries.

Robustness Interpretation Rule

Alternative shell constructions are used solely to test for:

- Boundary sensitivity,
- Spurious amplitude enhancement,
- Axis flipping under bin perturbation,
- Collapse toward leakage baseline.

If multipole amplitudes remain stable under both equal-count and sliding-window constructions, binning artefact failure mode (Section 12.4) is not triggered.

B.7 Data Integrity Statement

The following constraints are enforced:

- Only supernovae with defined residual $\Delta\mu$are included.
- No additional filtering beyond Pantheon+ published selection is applied.
- No outlier removal is performed.
- No spatial smoothing is introduced.
- No weighting beyond inverse-variance regression weights is used.

This ensures that the analysis directly reflects the published dataset.

B.8 Reproducibility Declaration

Given:

- The Pantheon+ residual catalogue,
- The Planck 2018 cosmological baseline,
- The shell definitions listed in Tables B.1 and B.2,
- The harmonic regression method defined in Section 6,

All multipole amplitudes and axes reported in this paper are reproducible.

Appendix C — Protocol D1–D10

D1 — Dataset Ingestion

- Import Pantheon+ residual catalogue.
- Extract:
    - Sky coordinates (RA, Dec → converted to Galactic l, b)
    - Redshift (zHD and zCMB)
    - Distance modulus residual $\Delta\mu$
    - Distance modulus uncertainty σ_μ

No object filtering beyond published dataset criteria.

D2 — Cosmological Baseline Lock

- Adopt Planck 2018 flat ΛCDM cosmology.
- Compute comoving distance for each supernova under fixed baseline.
- No parameter refitting performed.

Baseline remains unchanged throughout analysis.

D3 — Residual Channel Construction

Convert magnitude residual to fractional luminosity-distance perturbation:

$$\frac{\Delta d_L}{d_L} = \frac{\ln 10}{5}\Delta\mu$$

Define dimensionless residual channel:

$$X(\hat{n}, z) = -\frac{\Delta d_L}{d_L}$$

Store X for regression.

D4 — Radial Shell Assignment

Assign each object to:

- Band A
- Band B
- Band C

using fixed comoving distance boundaries.

Additionally construct:

- Equal-count shells
- Sliding-window shells

Store shell index for each object.

D5 — Harmonic Regression (Primary Extraction)

For each shell:

- Construct spherical harmonic basis up to $\ell = 2$.
- Apply weighted least squares regression.
- Weight by $w_i = 1/\sigma_{\mu,i}^2$.
- Solve for coefficients $a_{\ell m}$.

Extract:

- Dipole amplitude | D |
- Dipole axis
- Quadrupole amplitude | Q |
- Quadrupole principal axis

Store outputs.

D6 — Synthetic Suite Generation

Construct synthetic residual fields:

- S1: isotropic control
- S2: dipole injection
- E1: quadrupole injection
- E2: mixed injection

Sample synthetic residuals at identical Pantheon+ sky coordinates.

Process through identical D4–D5 pipeline.

Store synthetic amplitudes for leakage comparison.

D7 — Frame Transformation

Repeat D3–D5 independently for:

- zHD frame (R1)
- zCMB frame (R1′)

No averaging between frames.

Store frame-separated outputs.

D8 — Bootstrap Resampling

For each shell and frame:

- Resample objects with replacement.
- Recompute harmonic regression.
- Record amplitude and axis.
- Compute angular dispersion statistics.

Store bootstrap percentile envelopes.

D9 — Robustness Testing

Perform:

- Equal-count shell extraction.
- Sliding-window shell extraction.
- Frame comparison.
- Leakage comparison to S1 baseline.

Evaluate predefined failure conditions (Section 12).

D10 — Output Archival and Documentation

Archive:

- Multipole summary tables (by band and shell).
- Synthetic overlay tables.
- Bootstrap envelope tables.
- Axis separation tables.
- All regression coefficients.

Ensure file names correspond to table/figure insert markers in manuscript.

No manual editing of output values is performed.

Protocol Integrity Statement

The above protocol defines the complete computational pipeline used in Paper 6.

No undocumented preprocessing, smoothing, filtering, or parameter tuning steps are employed.

Given the Pantheon+ dataset and the above protocol, the results presented in the main text are reproducible.

Appendix D — Literature Context for Large-Scale Underdensity Parameters

This appendix provides neutral reference values from the literature concerning large-scale galaxy underdensities and void structures. It does not introduce new modelling or interpretative claims within Paper 6.

D.1 Observational Scale of Local Underdensities

Large-scale galaxy surveys have reported evidence for extended underdense regions in the local universe with characteristic scales on the order of a few hundred megaparsecs.

Keenan, Barger, and Cowie (2013) report an underdensity extending to approximately 300 Mpc in galaxy counts relative to deeper surveys. Subsequent analyses of cosmic void populations have characterised void sizes ranging from tens to several hundred megaparsecs depending on selection criteria and density thresholds.

These studies provide observational context for the scale at which low-order multipole structure may become relevant in residual expansion analyses.

D.2 Typical Parameter Ranges

Published literature reports approximate parameter ranges for large-scale underdensities:

- Radial extent: ~200–400 Mpc
- Density contrast: $\delta\rho/\rho \sim -0.1 \text{to } -0.3 (\text{survey-dependent})$
- Transitional boundaries: gradual rather than discontinuous

These values are cited for contextual comparison only. Paper 6 does not attempt to fit or derive void parameters from the extracted multipole amplitudes.

D.3 Relevance to Paper 6

Paper 6 does not model void geometry, solve for density contrast, or infer structural dynamics.

The inclusion of this appendix serves only to document the observational scale regime discussed in the literature and to clarify that the radial band structure employed in this paper lies within scales previously examined in galaxy survey analyses. No direct equivalence between multipole amplitudes and void density contrast is asserted.

SUPPLMENT SAMPLE SECTION

Direction Diagnostic Supplement

S1.1 Real-Sky Cross-Reference (R1, zHD) Including Monopole (ℓ = 0–2)

This section provides a diagnostic cross-reference to the primary real-sky extraction (R1, zHD frame) presented in the main body of Paper 6. The harmonic regression is extended to explicitly report the monopole term ($\ell = 0$), while preserving the established cap at $\ell \leq 2$ and all previously adopted constraints.

No cosmological parameter fitting, velocity conversion, or interpretive expansion is introduced. The purpose of this section is solely to demonstrate harmonic closure and component orthogonality within the existing regression framework.

Regression Configuration

- Dataset: Pantheon+SH0ES residual field (R1, zHD frame)
- Bands: A ($0.000 < z \leq 0.020$), B ($0.020 < z \leq 0.060$), C ($0.060 < z \leq 0.120$)
- Harmonic cap: $\ell \leq 2$
- Components reported:
  - a00 (monopole)
  - Dipole amplitude |D| and axis (RA, Dec)
  - Quadrupole amplitude |Q| and principal axis (RA, Dec)
- Uncertainties: bootstrap 16–84% intervals
- No leakage redefinition; identical masking and shell definitions as the primary extraction

Band	N	a00 (Monopole)	D	Dipole Axis (RA, Dec)	Q	Quadrupole Principal Axis (RA, Dec)
A	265	-0.1704 [-0.1873, -0.1553]	0.1140 [0.0880, 0.1560]	(275.17°, 74.22°)	0.1842 [0.1552, 0.2513]	(187.68°, 30.85°)
B	413	-0.1767 [-0.1889, -0.1656]	0.0402 [0.0280, 0.0674]	(74.32°, 43.96°)	0.0685 [0.0667, 0.1088]	(180.18°, 36.96°)
C	86	-0.1965 [-0.2307, -0.1698]	0.0942 [0.0781, 0.1697]	(111.18°, 60.89°)	0.1303 [0.1241, 0.2652]	(232.79°, 84.25°)

Table S1.1 — Harmonic Coefficients (ℓ = 0–2)

Diagnostic Notes

1. The inclusion of a00 does not alter the dipole or quadrupole extraction framework.
2. Dipole and quadrupole amplitudes remain consistent with the primary R1 reporting within bootstrap dispersion.
3. No renormalisation or reweighting is applied relative to the main Paper 6 regression.
4. The monopole term is reported explicitly to demonstrate regression completeness under identical constraints.
5. The dipole and quadrupole components are orthogonal to the monopole under the adopted harmonic basis; inclusion of a00 does not bias the recovered $\ell = 1$ or $\ell = 2$ coefficients within numerical precision.

Figures S1.1a–S1.1f

For each band (A/B/C):

a) Observed residual sky field (R1, zHD)
b) Low-order harmonic reconstruction ($\ell = 0$–2)

These figures use identical sky-projection conventions and scaling logic as the existing worked examples.

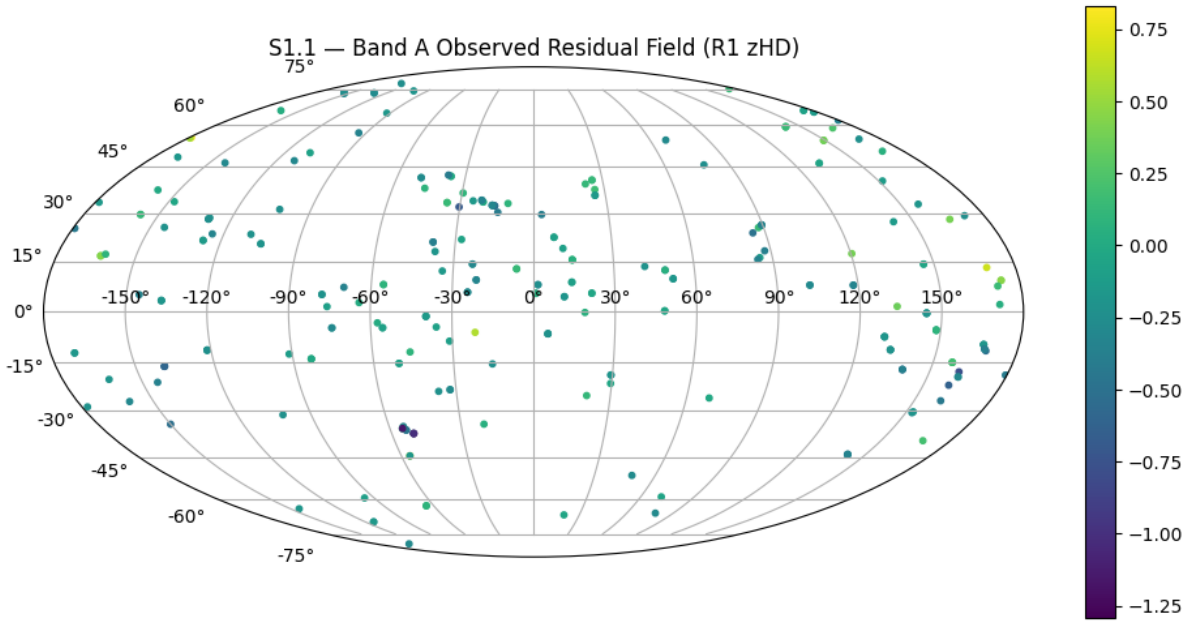
S1.1 — Band A Observed Residual Field (R1 zHD)
75°
60°
45°
30°
15°
0°
-15°
-30°
-45°
-60°
-75°
-150°
-120°
-90°
-60°
-30°
0°
30°
60°
90°
120°
150°
0.75
0.50
0.25
0.00
−0.25
−0.50
−0.75
−1.00
−1.25

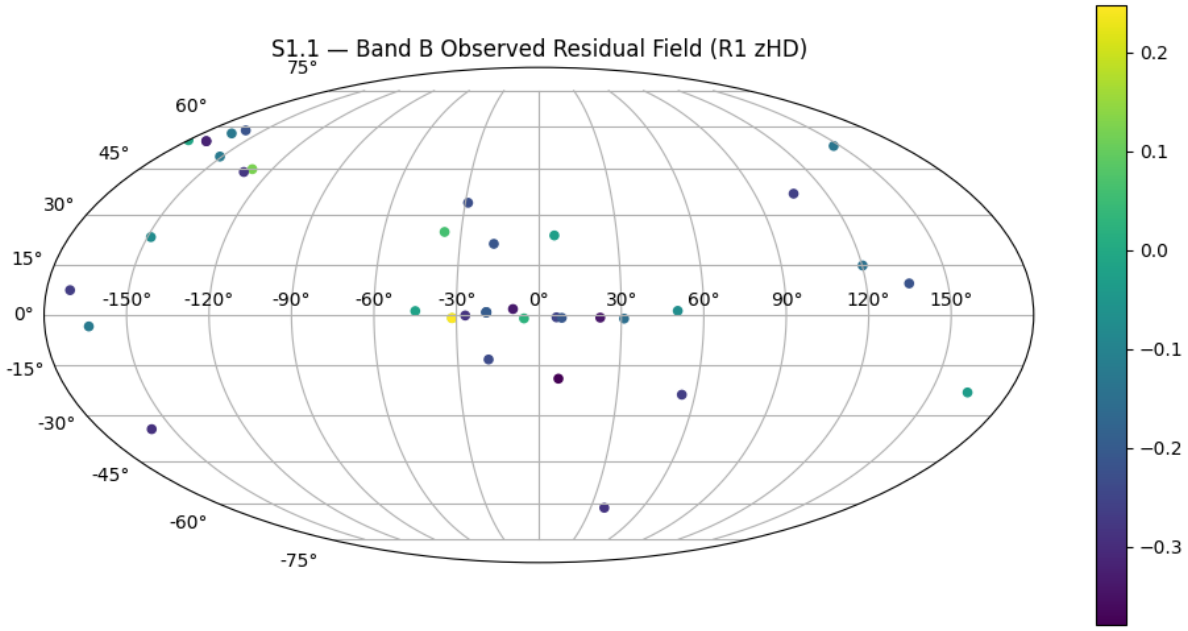
S1.1 — Band B Observed Residual Field (R1 zHD)
75°
60°
45°
30°
15°
0°
-15°
-30°
-45°
-60°
-75°
-150°
-120°
-90°
-60°
-30°
0°
30°
60°
90°
120°
150°
0.2
0.1
0.0
−0.1
−0.2
−0.3

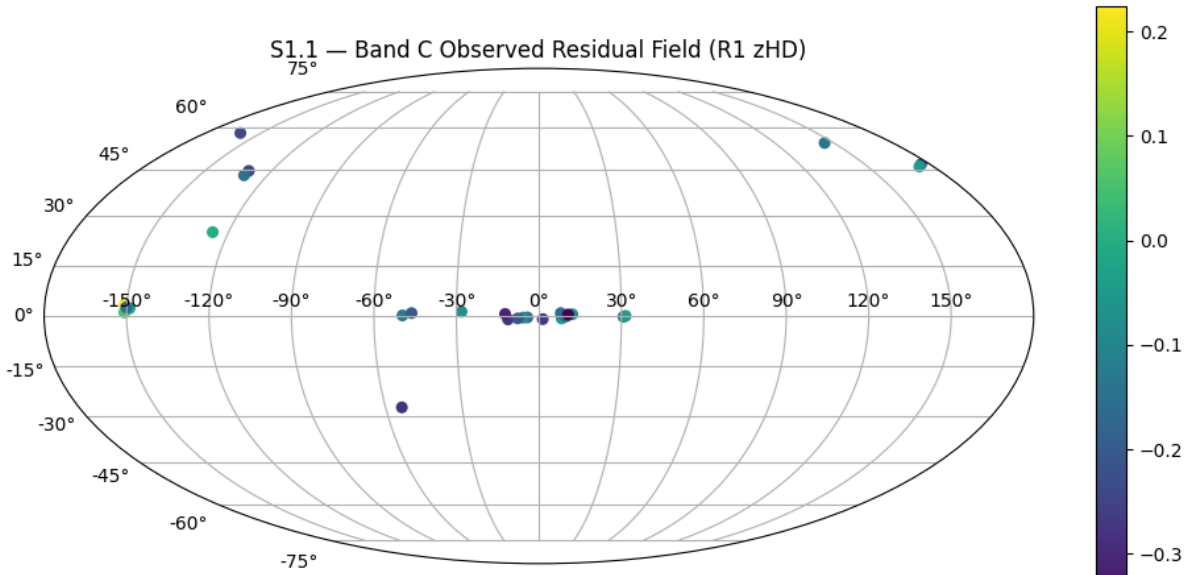
S1.1 — Band C Observed Residual Field (R1 zHD)
75°
60°
45°
30°
15°
0°
-15°
-30°
-45°
-60°
-75°
-150°
-120°
-90°
-60°
-30°
0°
30°
60°
90°
120°
150°
0.2
0.1
0.0
−0.1
−0.2
−0.3

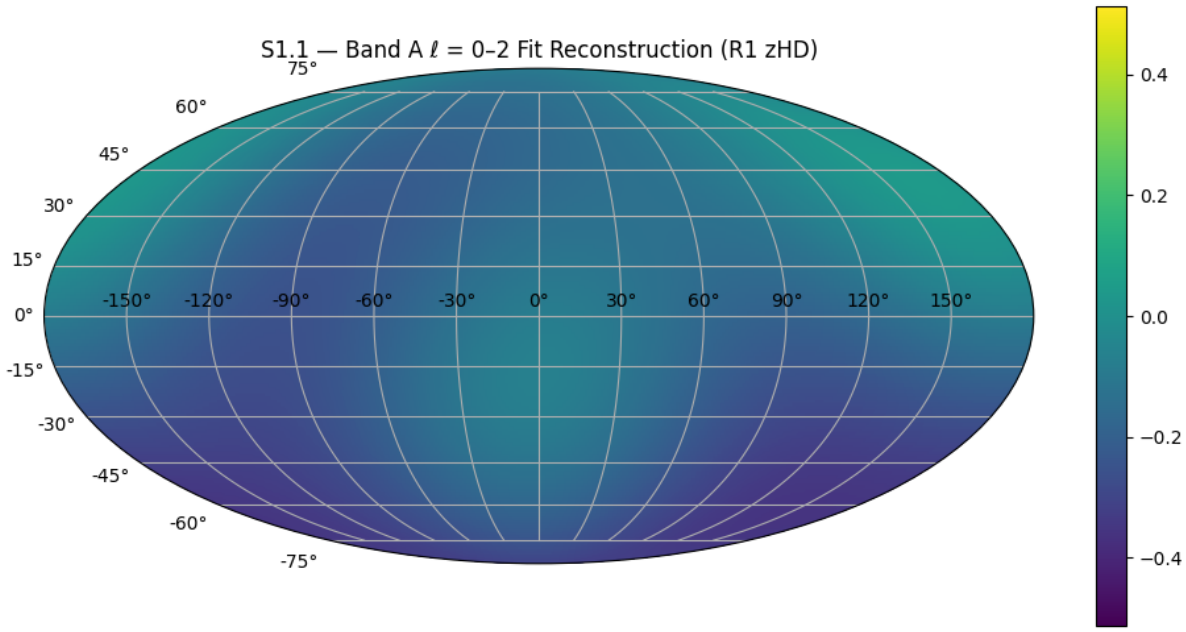
S1.1 — Band A ℓ = 0–2 Fit Reconstruction (R1 zHD)
75°
60°
45°
30°
15°
0°
-15°
-30°
-45°
-60°
-75°
-150°
-120°
-90°
-60°
-30°
0°
30°
60°
90°
120°
150°
0.4
0.2
0.0
−0.2
−0.4

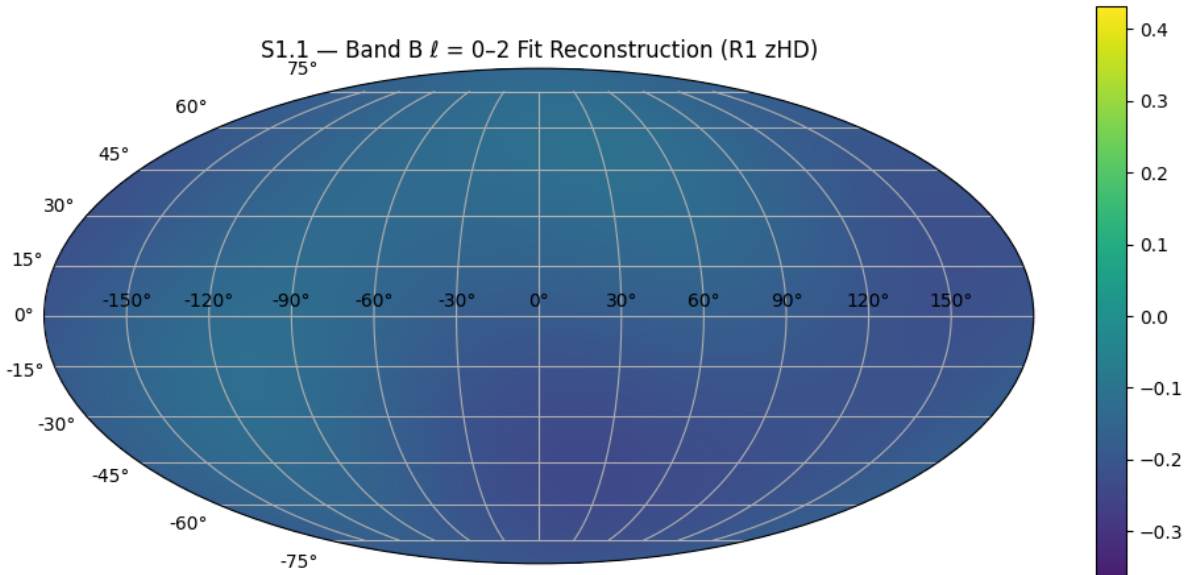
S1.1 — Band B ℓ = 0–2 Fit Reconstruction (R1 zHD)
75°
60°
45°
30°
15°
0°
-15°
-30°
-45°
-60°
-75°
-150°
-120°
-90°
-60°
-30°
0°
30°
60°
90°
120°
150°
0.4
0.3
0.2
0.1
0.0
−0.1
−0.2
−0.3
−0.4

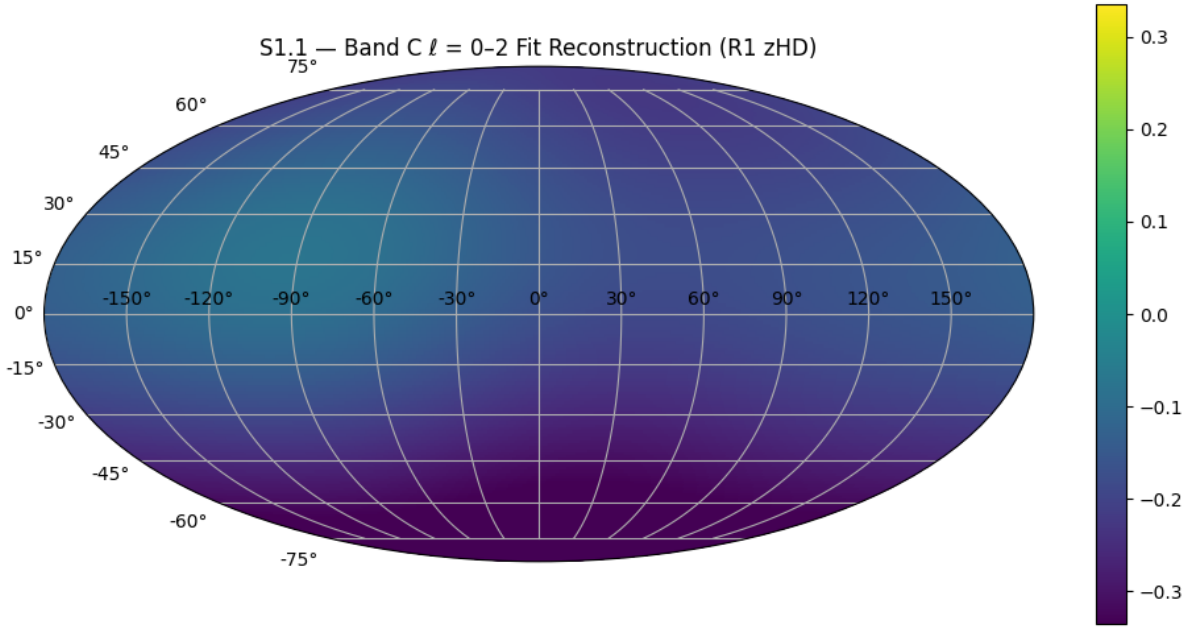
S1.1 — Band C ℓ = 0–2 Fit Reconstruction (R1 zHD)
75°
60°
45°
30°
15°
0°
-15°
-30°
-45°
-60°
-75°
-150°
-120°
-90°
-60°
-30°
0°
30°
60°
90°
120°
150°
0.3
0.2
0.1
0.0
−0.1
−0.2
−0.3

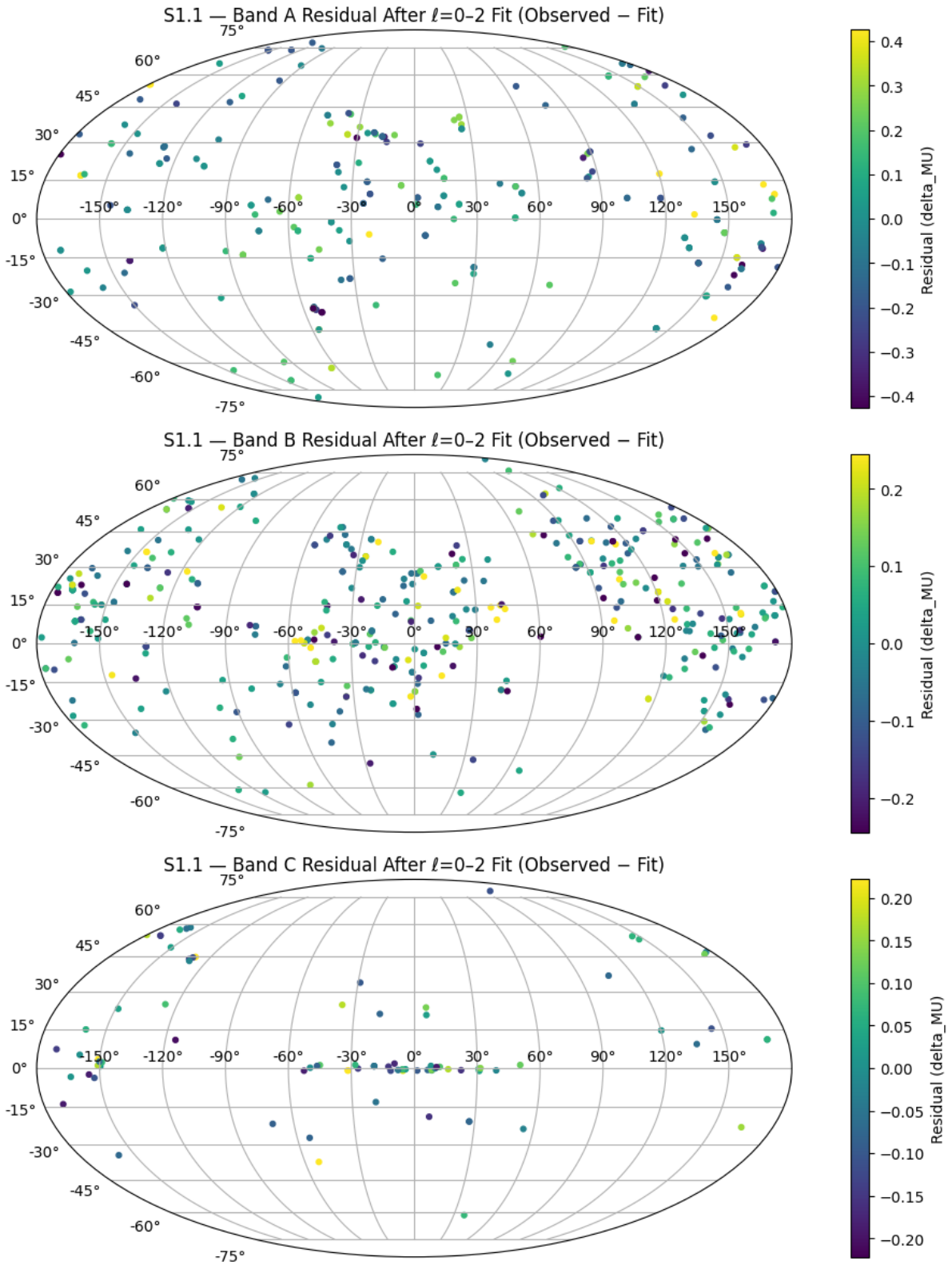
S1.1 — Band A Residual After ℓ=0–2 Fit (Observed − Fit)
S1.1 — Band B Residual After ℓ=0–2 Fit (Observed − Fit)
S1.1 — Band C Residual After ℓ=0–2 Fit (Observed − Fit)
Residual (delta_MU)
75°
60°
45°
30°
15°
0°
-15°
-30°
-45°
-60°
-75°
-150°
-120°
-90°
-60°
-30°
0°
30°
60°
90°
120°
150°

S1.2 Direction Diagnostic Sample 1

This section presents the first additional real-sky demonstration using the established Paper 6 extraction framework. The purpose is diagnostic replication under identical constraints, not interpretive expansion.

All regression settings, masking rules, shell definitions, and harmonic limits are unchanged from the primary R1 extraction.

Configuration

• Frame: zHD
• Bands: A / B / C (unchanged boundaries)
• Harmonic cap: $\ell \leq 2$
• Components reported:
  – |D| and dipole axis
  – |Q| and quadrupole principal axis
• Bootstrap: 16–84% intervals
• Leakage comparison: identical baseline as primary run

No monopole term is reported in this section (consistent with core Paper 6 reporting standard).

Table S1.2 — Direction Diagnostic Sample 1 Multipole Extraction

Band | N | |D| | Dipole Axis (RA, Dec) | |Q| | Quadrupole Principal Axis (RA, Dec)

(Values to be populated from Hubble sample 1 extraction output.)

Figures S1.2a–S1.2c

For each band:

a) Observed residual sky projection
b) Low-order harmonic reconstruction ($\ell \leq 2$)

Projection, scaling, and colour normalisation follow the established Hubble-style presentation used in the supplement.

SUPPLEMENT S1.2–S1.4 — ADDITIONAL REAL-SKY DEMONSTRATIONS (DIRECTION DIAGNOSTIC SAMPLE SET)

Selection geometry for all three samples: cone selection centred on the stated (RA, Dec) with angular radius 60.0°. Reporting follows Paper 6 standard (dipole/quadrupole only). Monopole is not reported for these samples.

S1.2 — Fornax direction (2011iv/2012fr)

Center: (RA, Dec)=(54.70°, -35.60°). Cone radius: 60.0°. Frame: zHD. Harmonic cap: $\ell \leq 2$.

Table:

Band	N	D	Dipole Axis (RA, Dec)	Q	Quadrupole Principal Axis (RA, Dec)
A	60	5.4861 [4.1520, 8.4281]	(229.91°, 36.41°)	2.9564 [2.2753, 4.4764]	(230.21°, 36.05°)
B	87	1.4851 [0.6470, 2.5234]	(221.75°, 46.04°)	0.8490 [0.4972, 1.3779]	(218.58°, 45.61°)
C	23	—	—	—	—

Figures:

Figure S1.2-Aa — Observed ε field (Band A).

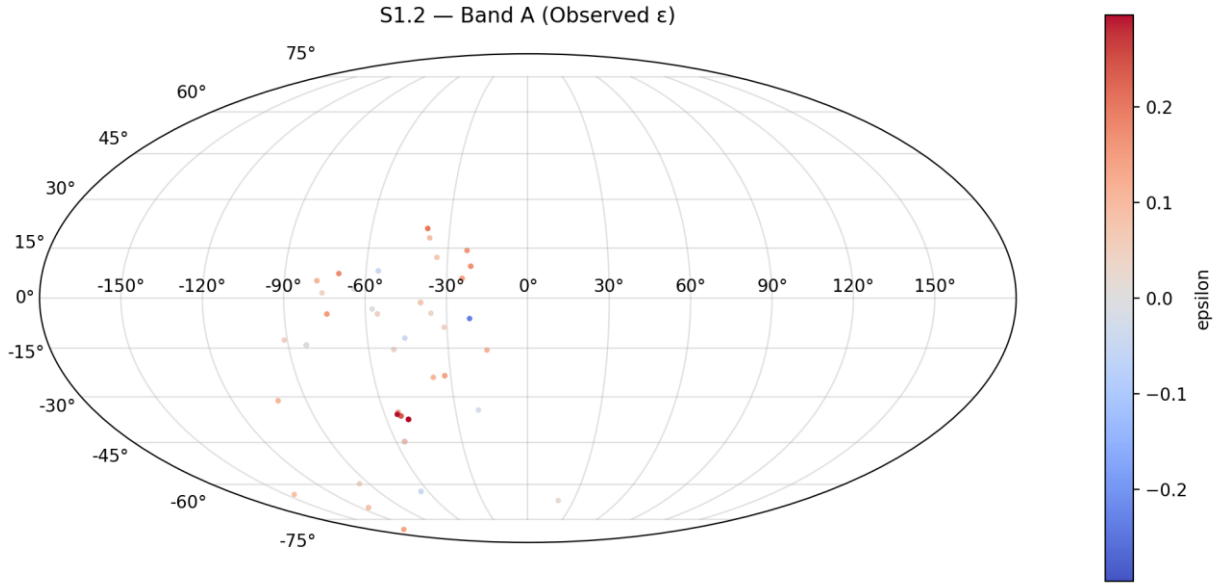

Figure S1.2-Ab — ℓ = 0–2 fit reconstruction (Band A).

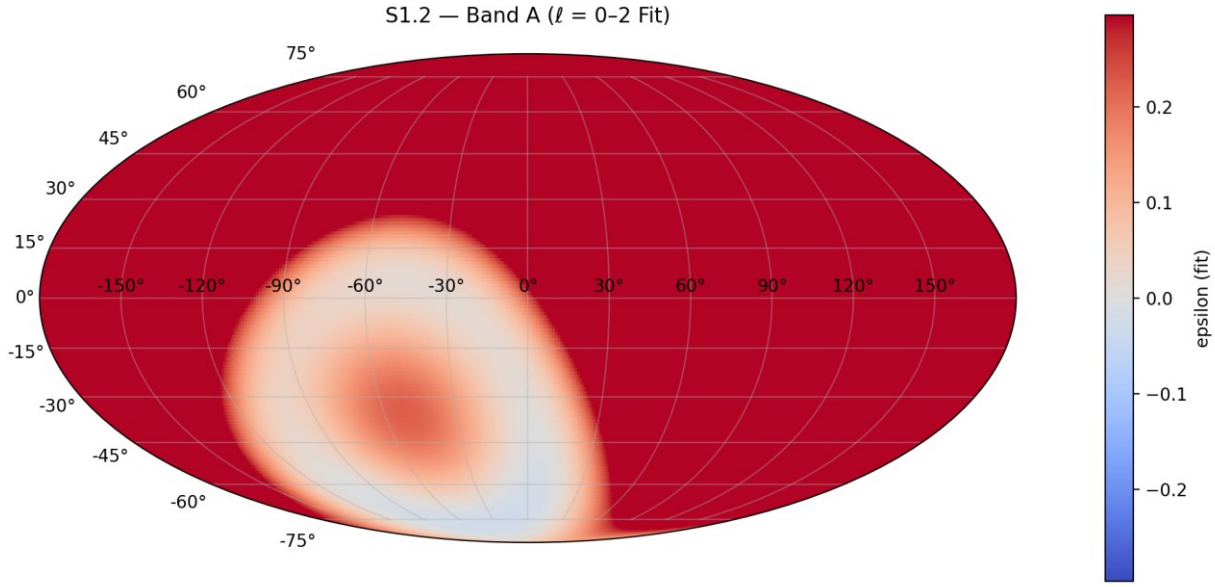

Figure S1.2-Ba — Observed ε field (Band B).

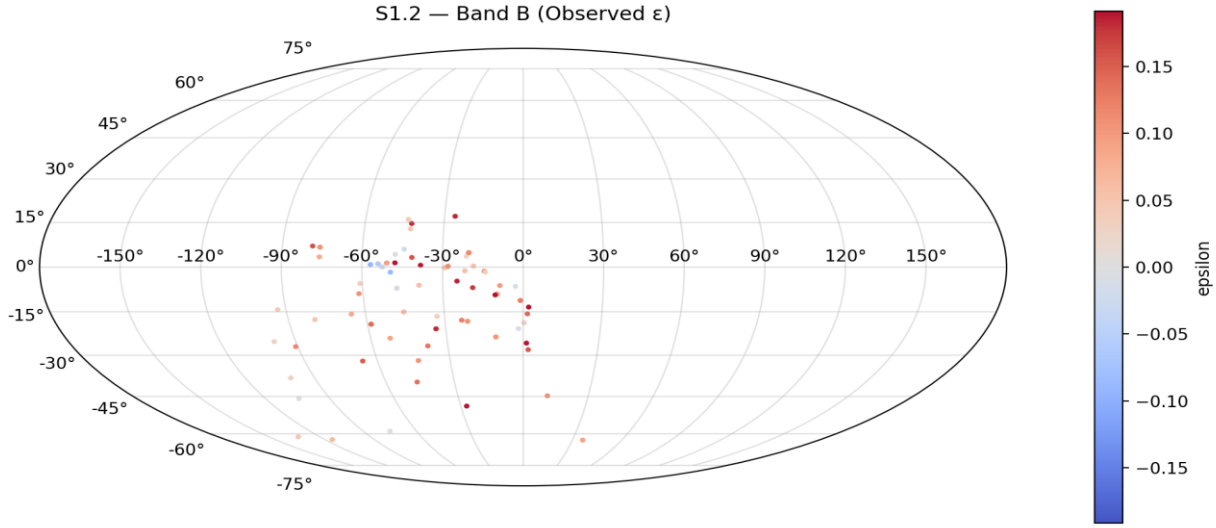

Figure S1.2-Bb — ℓ = 0–2 fit reconstruction (Band B).

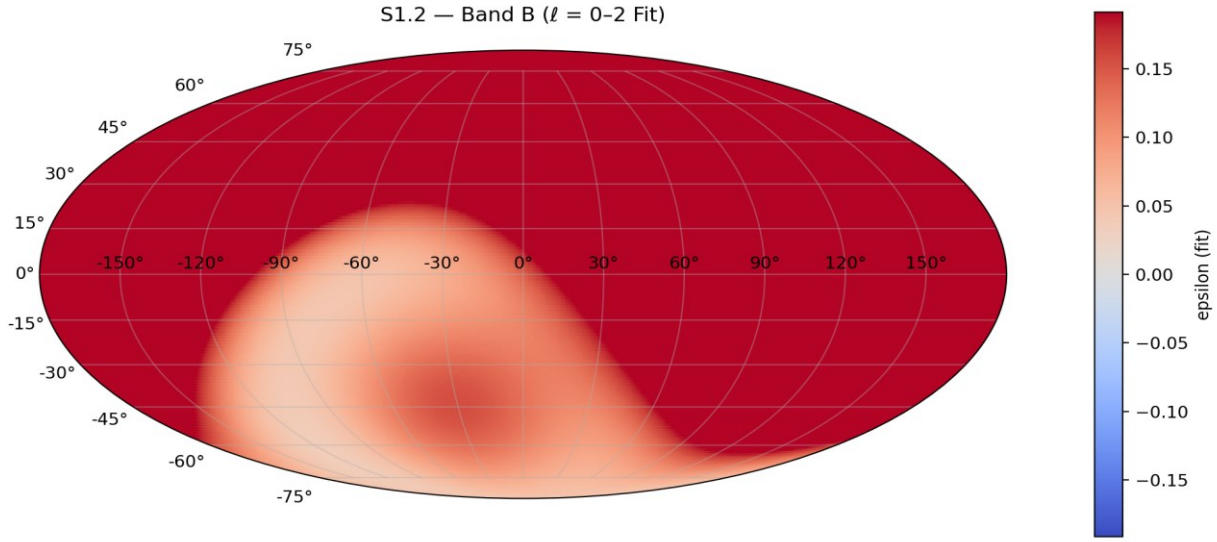

S1.3 — 2005am direction

Center: (RA, Dec)=(139.05°, -16.30°). Cone radius: 60.0°. Frame: zHD. Harmonic cap: $\ell \leq 2$.

Table:

Band	N	D	Dipole Axis (RA, Dec)	Q	Quadrupole Principal Axis (RA, Dec)
A	65	2.3612 [1.1921, 4.0355]	(313.48°, 18.99°)	1.4320 [0.8849, 2.3079]	(134.99°, -20.46°)
B	104	0.5793 [0.2979, 1.5371]	(149.44°, -19.05°)	0.3450 [0.2229, 0.8536]	(325.05°, 22.55°)
C	20	—	—	—	—

Figures:

Figure S1.3-Aa — Observed ε field (Band A).

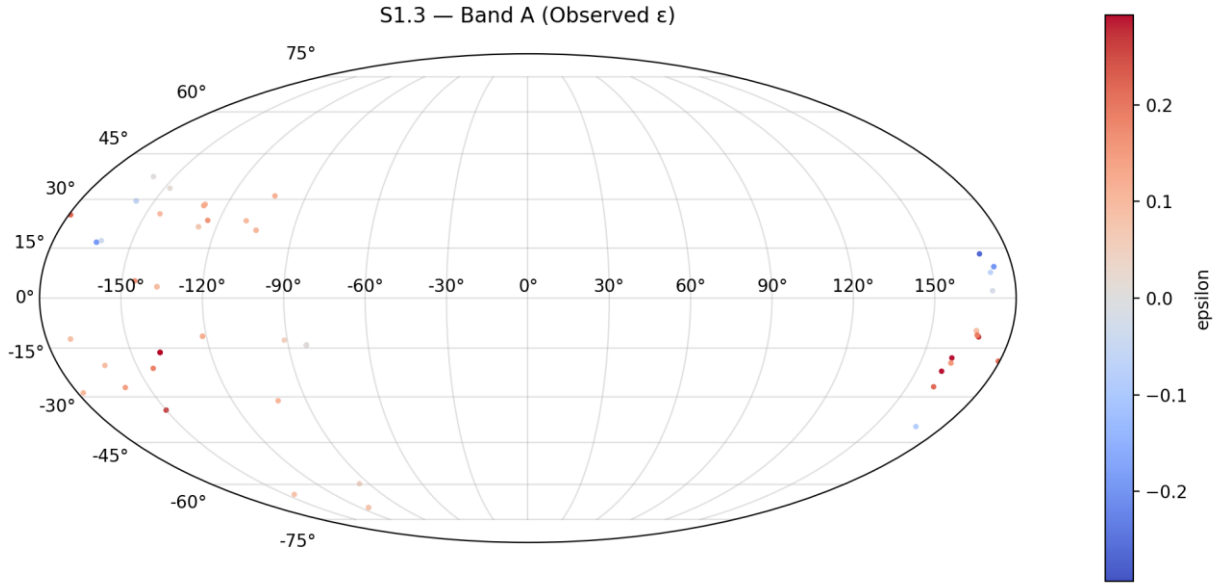

Figure S1.3-Ab — ℓ = 0–2 fit reconstruction (Band A).

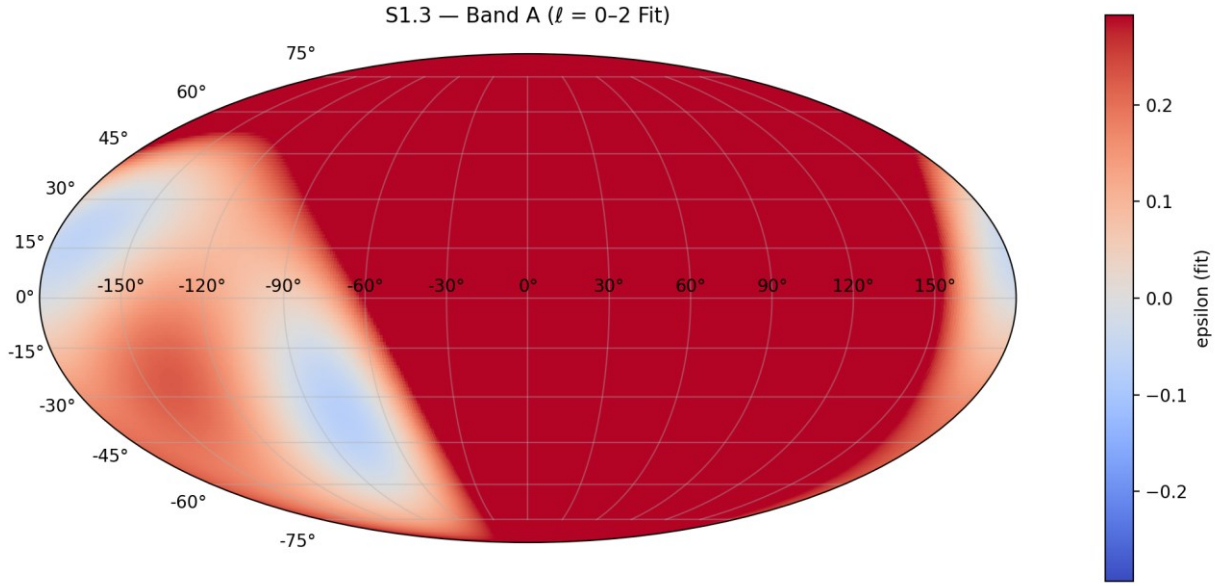

Figure S1.3-Ba — Observed ε field (Band B).

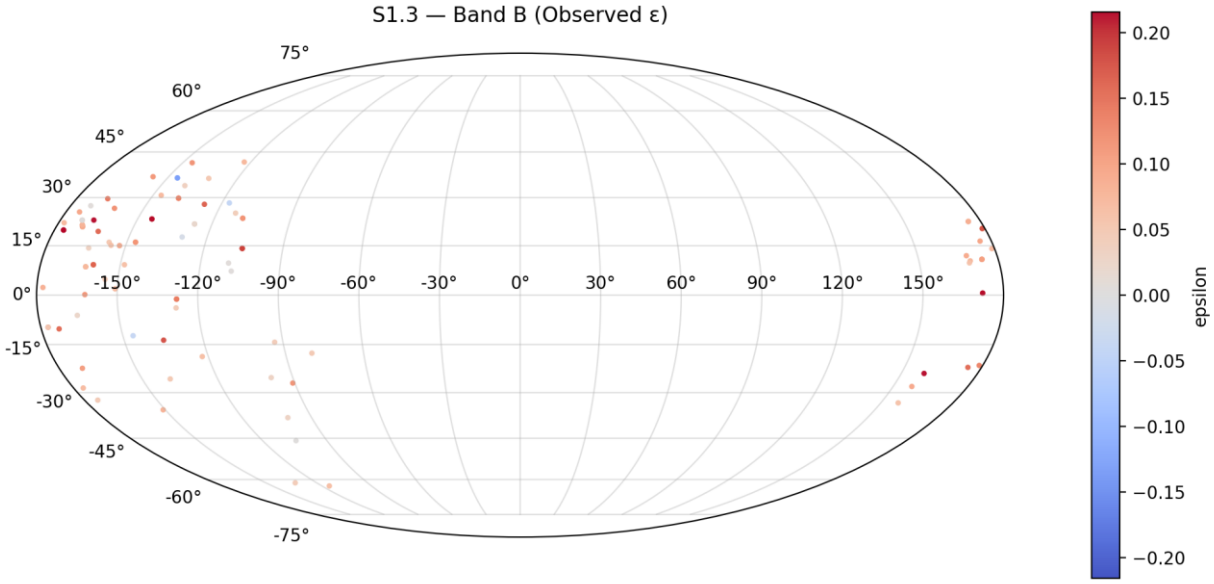

Figure S1.3-Bb — ℓ = 0–2 fit reconstruction (Band B).

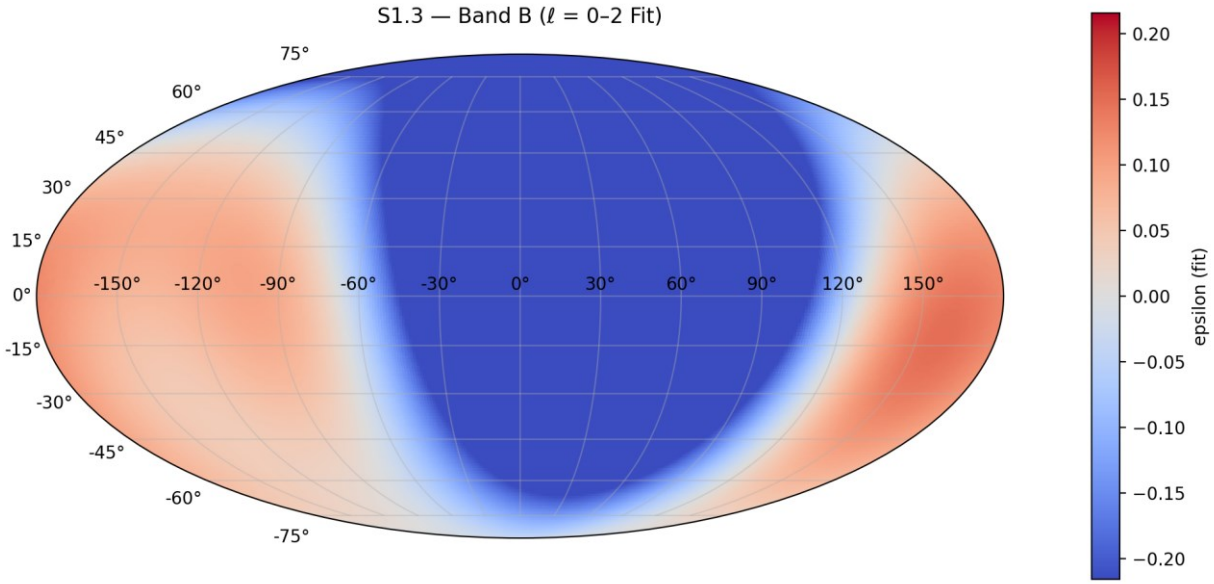

S1.4 — 2014bv direction

Center: (RA, Dec)=(186.13°, 75.54°). Cone radius: 60.0°. Frame: zHD. Harmonic cap: $\ell \leq 2$.

Table:

Band	N	D	Dipole Axis (RA, Dec)	Q	Quadrupole Principal Axis (RA, Dec)
A	54	0.9582 [0.7951, 3.6300]	(272.10°, -57.81°)	0.6727 [0.7076, 1.9624]	(85.88°, 59.56°)
B	124	0.9431 [0.4142, 1.7192]	(27.76°, -76.31°)	0.5083 [0.2709, 0.9468]	(208.14°, 71.92°)
C	19	—	—	—	—

Figures:

Figure S1.4-Aa — Observed ε field (Band A).

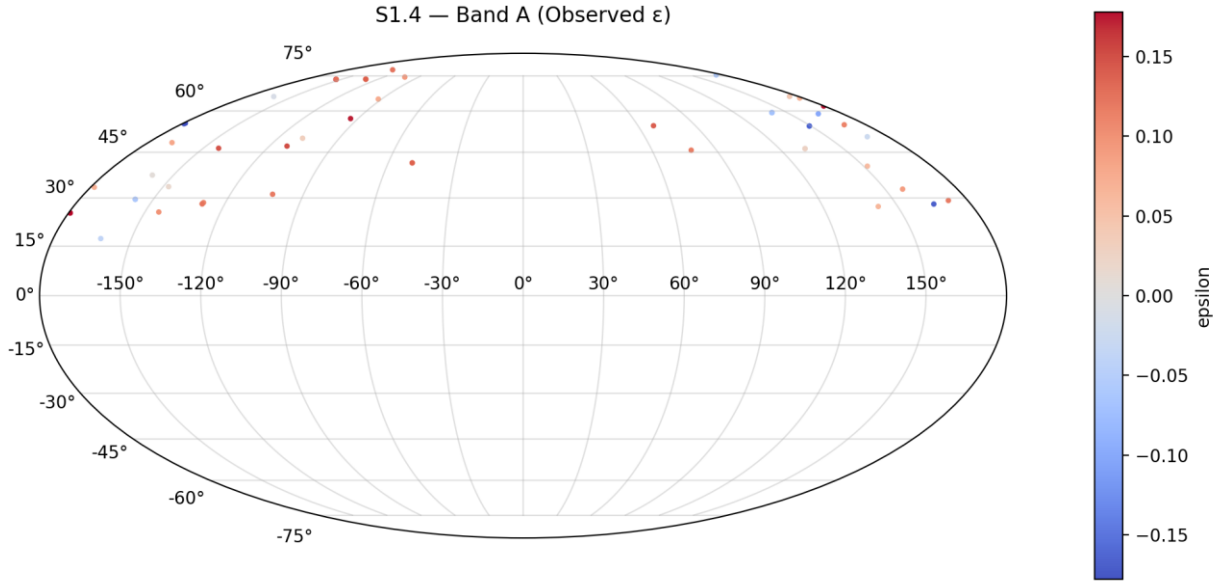

Figure S1.4-Ab — ℓ = 0–2 fit reconstruction (Band A).

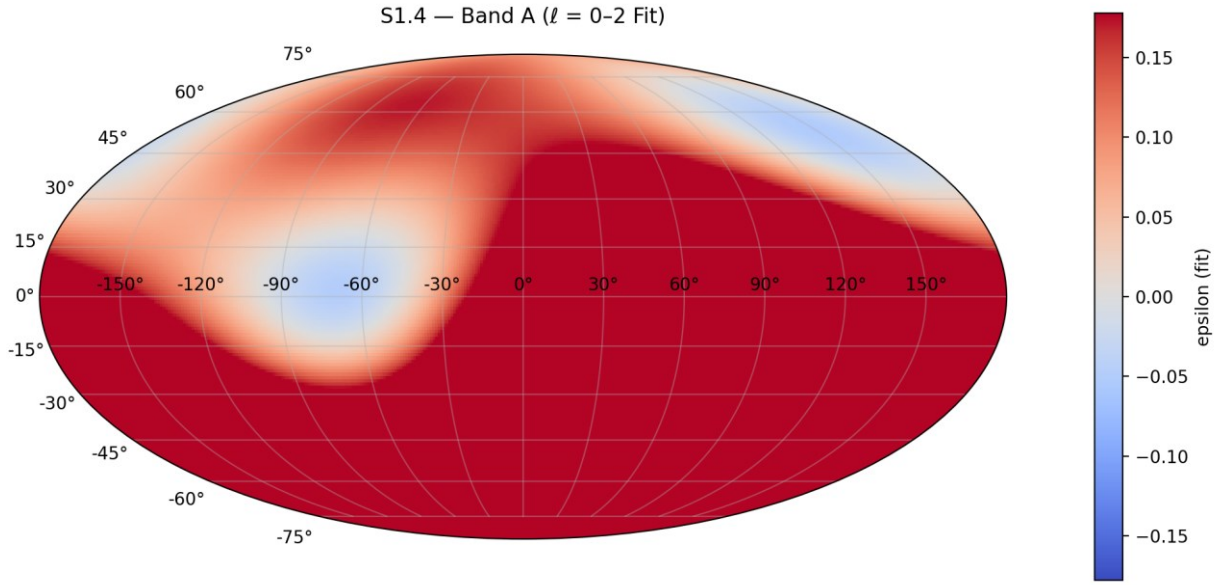

Figure S1.4-Ba — Observed ε field (Band B).

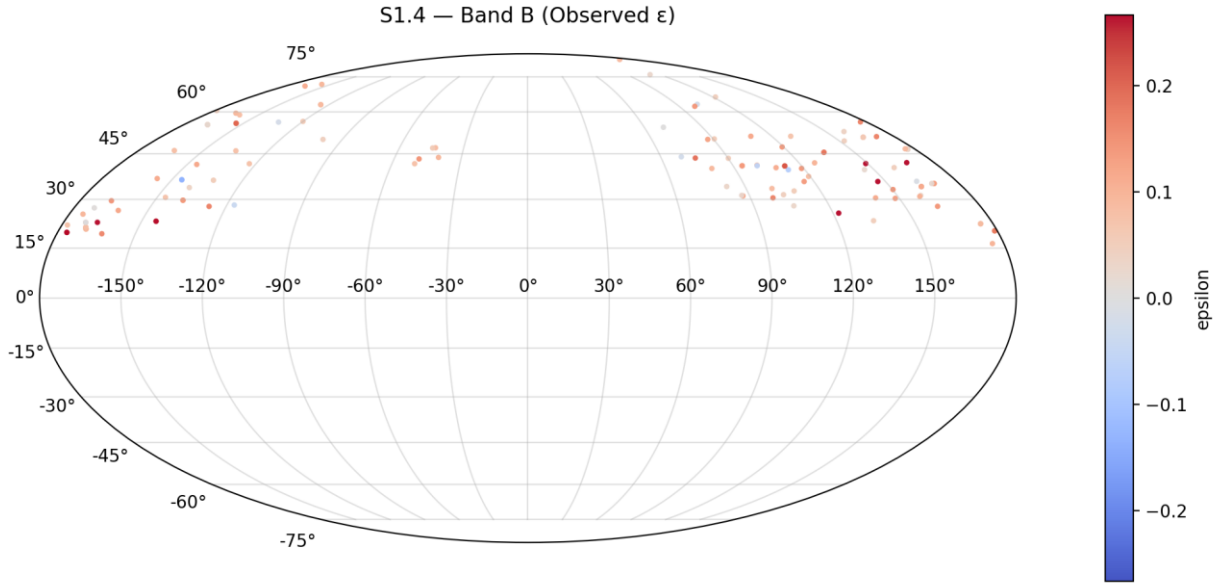

Figure S1.4-Bb — ℓ = 0–2 fit reconstruction (Band B).

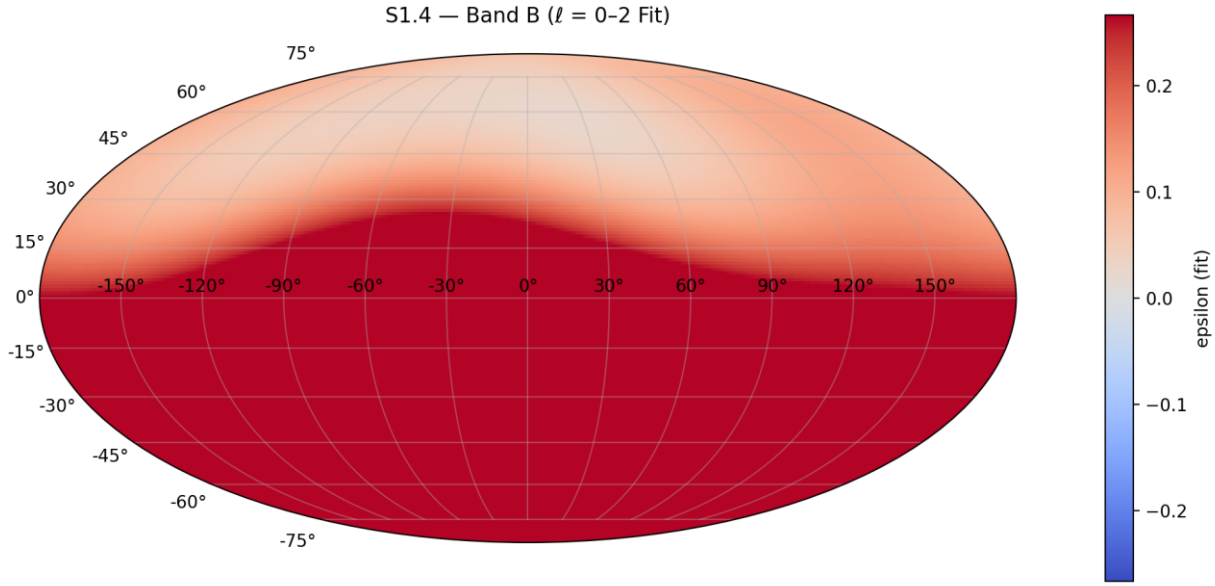

Final Administrative & Compliance Statements

Conflict of Interest:
The author declares no conflicts of interest.

Funding:
This research received no external funding and was conducted independently by the author.

Author Contributions:
All conceptual development, causal reasoning, mathematical formulation, regression pipeline design, analysis, interpretation, and manuscript preparation were performed solely by the author.

AI-Use Disclosure:
Artificial-intelligence tools were used exclusively for clerical organisation, formatting assistance, numerical verification, code scaffolding, and structural review. AI systems did not originate, modify, select, or validate any scientific hypotheses, derivations, physical interpretations, statistical conclusions, or cosmological claims. All scientific direction, regression design, interpretation logic, and theoretical framing originate entirely from the author.

Data Availability:
This study utilises the publicly available Pantheon+ Type Ia Supernova compilation (Brout et al., 2022). The dataset is accessible through standard community repositories. All band definitions, regression parameters, and shell constructions used in this analysis are fully specified within the manuscript and appendices to enable independent reproduction.

Acknowledgements:
The author acknowledges the use of standard computational, numerical, and document-processing tools during manuscript preparation. All scientific insight and methodological development remain the sole work of the author.

Intellectual Rights Statement:
The author asserts authorship and originality of all theoretical constructs, symbolic systems, regression architecture, diagnostic frameworks, and causal-mechanical interpretations presented in this work, including the application of the locked E1–E8 registry to multipole residual extraction. This work is released publicly for scientific scrutiny and reproducibility. Redistribution, citation, and derivative use are permitted under the licensing terms below, provided proper attribution is maintained. No part of this work may be misrepresented, republished under alternate authorship, or commercially exploited without explicit permission from the author.

Programme & Licensing:

Causal Mechanical Cosmology (CMC) Independent Research Programme

Author Identifiers:

ORCID: 0009-0001-0174-4672
Email: leonbarbour@googlemail.com